Probing Color-Singlet Exchange in $p\bar{p}$ Collisions at $\sqrt{s} = 630$ GeV and 1800 GeV

The members of the Committee approve the doctoral dissertation of Jill Perkins

Paul Draper
Supervising Professor

Andrew P. White

Ransom Stephens

Truman D. Black

Asok Ray

Dean of the Graduate School

To life, love, and exploration

Probing Color-Singlet Exchange in $p\bar{p}$ Collisions at $\sqrt{s} = 630$ GeV and 1800 GeV

by

JILL PERKINS

Presented to the Faculty of the Graduate School of

The University of Texas at Arlington in Partial Fulfillment

of the Requirements

for the Degree of

DOCTOR OF PHILOSOPHY

THE UNIVERSITY OF TEXAS AT ARLINGTON

May 1998

ACKNOWLEDGMENTS

The analysis presented in this thesis has been possible out of a large collaborative effort of all the people who have contributed to DØ since its conception. I acknowledge those who contributed years of thought and energy to design, build, and test the detector and the software tools needed to begin such a large scale experiment. In addition, I acknowledge those who have contributed to the maintenance and growth of all facets of the experiment. I feel very fortunate to have had the opportunity to work in such a diverse collaboration, and I am thankful for the good fortune of meeting some amazing people over these years.

In particular, I have abundant appreciation for my rapidity gap colleagues. I thank Andrew Brandt for his direction, enthusiasm, and support. I thank Brent May for contributing his knowledge and patience. I am deeply grateful to Tracy Taylor Thomas for her many contributions to this analysis. This analysis mirrors her's in many ways and is an extension of the work she has done on probing the nature of color-singlet exchange. I thank this group along with the QCD group for creating an environment of encouragement, interest, and support.

I especially thank my advisor Paul Draper who recruited me into high energy physics as an undergraduate. I thank him for his undying support and encouragement, and for helping me out beyond the call of duty. I acknowledge Paul for being a wonderful physics professor and for contributing quality to the education provided at my institution.

As head of the high energy group at UT Arlington, Andy White has lead a tremendous effort in getting our group started and supported over the years. I thank

him for this. I also thank Lee Sawyer who patiently tried to teach me everything he knows about high energy physics, DØ software, programming, and a list too long to reproduce here. Thanks Lee!

Over the years, I could not have survived the difficulty I made of this journey without the love and support of my friends and family. With the deepest appreciation, I thank them all. In particular, I praise Sean Fleming for being the wonderful man that he is. I thank Gordon Watts for his generosity and brotherly love. I acknowledge Julie Parizek for her enthusiasm, spunk, and divine wisdom. I gratefully appreciate Brent May whose contributions to this experience are greater than he or I can possibly comprehend. I honor my parents, Bobbie and George Perkins, for a lifetime of love, support, encouragement, guidance, inspiration, and for being the best parents any person could have. I am thankful that Otto and Enzo have travelled this long journey with me providing constant love and understanding.

This experience has been the most rewarding and insightful time of my life, and I have great appreciation for everyone that has participated in this adventure. I thank you all.

April 13, 1998

ABSTRACT

Probing Color-Singlet Exchange in $p\bar{p}$ Collisions at $\sqrt{s} = 630$ GeV and 1800 GeV

Publication No._____

Jill Perkins, Ph.D.

The University of Texas at Arlington, 1998

Supervising Professor: Paul Draper

Experimental results are presented from an analysis of events with rapidity gaps between high transverse momentum jets. The data were collected from $p\bar{p}$ collisions at $\sqrt{s} = 630$ GeV and 1800 GeV using the DØ Detector at Fermi National Accelerator Laboratory. Particle multiplicity distributions between jets with large pseudorapidity separation are measured using calorimeter tower and charged tracks information. The fraction of events with rapidity gaps between jets is a direct measurement of the fraction of color-singlet exchange. The rapidity gap fraction is measured as a function of the jet transverse energy, the rapidity separation between jets, parton x, and the center-of-mass energy. The results presented are inconsistent with those expected from the naive two-gluon model for color-singlet exchange.

TABLE OF CONTENTS

ACKNOWLEDGMENTS . . . . . **v**

ABSTRACT . . . . . **vi**

LIST OF FIGURES . . . . . **xii**

LIST OF TABLES . . . . . **xiii**

1 INTRODUCTION **1**

1.1 Overview of QCD 1

1.2 Invariant Phase Space 4

1.3 Color Flow and Particle Multiplicity 4

1.4 Color-Singlet Exchange Fraction 7

1.4.1 Survival Probability 8

1.5 Color-Singlet Models 9

1.5.1 Two-Gluon and BFKL 9

1.5.2 Soft Color Rearrangement 11

1.5.3 An Alternative Model 12

1.6 Previous Measurements 13

2 THE DØ EXPERIMENT **14**

2.1 The Fermilab Tevatron $p\bar{p}$ Collider 14

2.2 Coordinate Systems 16

2.3 The DØ Detector 18

2.4 The Central Tracking System 19
2.5 The Calorimeter 21
2.5.1 Central Calorimeter 25
2.5.2 End Calorimeters 25
2.5.3 Intercryostat Detectors 26
2.5.4 Calibration 26
2.5.5 Noise 27
2.6 Muon System 29
2.7 Triggering and Data Acquisition 29
2.7.1 Level Ø 30
2.7.2 Level 1 30
2.7.3 Level 2 30
2.8 Jet Reconstruction 31
2.8.1 Event Vertex 31
2.8.2 Jet Finding Algorithm 32
2.8.3 Jet Energy Scale 34

3 DATA SELECTION 35
3.1 Triggers 35
3.1.1 Level Ø and Level 1 35
3.1.2 Level 2 Filters 36
3.2 Offline Event Selection 36
3.2.1 Bad Run Removal 36
3.2.2 Calorimeter Noise Suppression 37
3.2.3 Jet Quality Cuts 37

3.2.4 Final Data Samples 38

4 MEASUREMENT OF THE RAPIDITY GAP FRACTION . . . 44

4.1 Methods for Measuring the Fraction 44

4.1.1 Negative Binomial Fit Method 45

4.1.2 Two-Dimensional Method 51

4.1.3 Background Estimation and Uncertainty 54

4.2 Corrections to the Fraction 58

4.2.1 Luminosity 58

4.2.2 Event Vertex 59

4.3 Systematics and Errors 61

5 RESULTS AND INTERPRETATIONS 65

5.1 Measurement of the Color-Singlet Fraction 65

5.1.1 Dependence on Tower Threshold 67

5.1.2 f_s from Central Tracking Multiplicity 70

5.1.3 f_s for 2-Jet Events 70

5.1.4 Color-Singlet Fraction from Two Dimensional Method 71

5.1.5 Interpretation of f_s 72

5.2 Color-Singlet Fraction Versus Jet E_T 73

5.2.1 Interpretation of f_s^{2-D} vs. Jet E_T 77

5.3 Color-Singlet Fraction Versus $\Delta\eta$ 78

5.3.1 Interpretation of f_s^{2-D} vs. $\Delta\eta$ 81

5.4 Color-Singlet Fraction Versus Parton x 81

5.4.1 Parton x of the $\Delta\eta$ Measurement 81

5.4.2 Various Parton x Definitions 83

5.4.3 Parton x for 630 GeV Data 85

5.4.4 Interpretation of f^{2-D} vs. Parton x 85

6 CONCLUSIONS **87**

BIBLIOGRAPHY **90**

LIST OF FIGURES

Figure Page

1.1. Feynman diagram of quark scattering via exchange of a gluon 2

1.2. Color exchange event topology 5

1.3. Color-singlet exchange event with a rapidity gap 6

1.4. Depiction of particle multiplicity distributions 7

1.5. Soft color rearrangement 12

2.1. Overview of the Fermilab accelerator complex 15

2.2. Coordinate Systems 17

2.3. An overview of the DØ detector 19

2.4. Components of the central tracking system 20

2.5. The DØ calorimeters 22

2.6. Calorimeter layer structure 24

3.1. EM calorimeter tower occupancy showing hot cells 37

3.2. Jet characteristics of final data sets 41

3.3. Event characteristics of final data sets 42

3.4. Detector event display for a rapidity gap event 43

3.5. Calorimeter energy deposition for a rapidity gap event 43

4.1. Fit of central calorimeter multiplicity for 1800 GeV data 47

4.2. Calorimeter multiplicity with full and leading edge NBD fit 48

4.3. Low multiplicity region with overlay of full and leading edge NBD fit 49

4.4. Calorimeter multiplicities for different luminosities 50

4.5. Calorimeter vs tracking multiplicity for 1800 GeV data 53

4.6. Central calorimeter multiplicity for same-side jet events 55

4.7. Calorimeter vs. tracking multiplicity for same-side data 56

4.8. Calorimeter and tracking multiplicity bins used in
the two-dimensional background estimation 57

4.9. The second factor of the luminosity correction 60

4.10. Fraction of single vertices versus luminosity for
630 GeV data 62

4.11. Fraction of single vertices versus luminosity for
1800 GeV data 63

5.1. NBD fits to central calorimeter multiplicities 66

5.2. Calorimeter multiplicities with different tower thresholds 68

5.3. Gap fraction vs. calorimeter tower threshold 69

5.4. Overlay of 1800 GeV calorimeter multiplicity with
270 MeV tower threshold to 630 GeV multiplicity 69

5.5. NBD fits to central tracking multiplicities 71

5.6. Central calorimeter multiplicities for three E_T samples 74

5.7. Two-dimensional fraction and background vs. jet E_T 75

5.8. Two-dimensional rapidity gap fraction vs. jet E_T 76

5.9. Two-dimensional fraction and background vs.
jet $\Delta\eta$ separation 79

5.10. Two-dimensional rapidity gap fraction vs.
jet $\Delta\eta$ separation 80

5.11. Two-dimensional rapidity gap fraction vs.
parton x from $\Delta\eta$ bins 82

5.12. Two-dimensional fraction vs. parton x
(four definitions) 84

5.13. Two-dimensional fraction vs. parton $\bar{x}$ at
630 and 1800 GeV 86

5.14. Two-dimensional fraction vs. parton $\bar{x}$ with 630 GeV
data normalized to 1800 GeV survival probability 86

LIST OF TABLES

Table Page

2.1. Typical calorimeter noise widths 28

3.1. Offline selection criteria 39

4.1. Gap fraction versus NBD fit starting bin at 1800 GeV 51

4.2. Gap fraction versus NBD fit starting bin at 630 GeV 51

4.3. Gap fraction versus NBD fit ending bin at 1800 GeV 52

4.4. Gap fraction versus NBD fit ending bin at 630 GeV 52

4.5. Systematic Error Sources 61

5.1. Characteristics of the two-dimensional rapidity gap fraction vs. jet E_T 77

5.2. Characteristics of the two-dimensional rapidity gap fraction vs. jet $\Delta\eta$ separation 78

CHAPTER 1

INTRODUCTION

High energy particle physics is the study of the fundamental particles of our universe and the fundamental forces that govern their interactions. The strong force, one of the four fundamental forces, is described within the Standard Model of particle physics by the theory of quantum chromodynamics (QCD). Hadrons (protons, neutrons, etc.) are composite particles constructed from point-like, color-charged constituents called partons (parts of hadrons). QCD describes how partons interact via the strong force and how they bind together to form hadrons.

1.1 Overview of QCD

Partons, quarks and gluons, interact via the exchange of color. Analogous to electric charge, color charge must be conserved. In contrast to electrically charged objects, colored objects are *confined*: partons cannot be observed as free particles since the force of attraction increases as the distance between them increases. Quarks can have one of three color charges (red(R), green(G), or blue(B)). Gluons can have one of eight ("color-octet") color-anticolor charge combinations. The color-symmetric gluon ($R\bar{R}+G\bar{G}+B\bar{B}$) is a "color-singlet" (no net color charge) and does not interact. A Feynman diagram of quark scattering via the exchange of a gluon is shown in figure 1.1. The strength of the "amplitude" for a given parton-parton scattering process is determined by the magnitude of charge (color factor, c) that each interacting

parton carries and the strong coupling constant α_s ($c_1 c_2 \alpha_s^2/2$). The amplitude is used to calculate the rate at which a scattering process will occur.

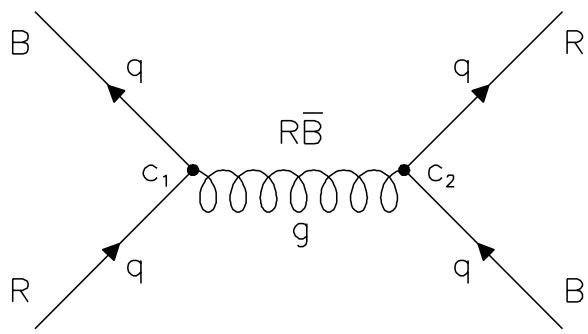

Figure 1.1. Feynman diagram of quark (q) scattering via the exchange of a gluon (g). The color flow through each vertex is represented by the assignment of a color factor c. Color charge is conserved throughout the process.

Within QCD, the quark-parton model [1] describes the structure of the proton in terms of its constituent partons. In hadron collisions with a large momentum transfer, the parton model assigns each parton within the hadron a fraction x of the total hadron momentum. Within this framework, it is the partons themselves which are involved in the collision. *Parton distribution functions* (pdf's) represent the parton's probability density of having a certain momentum fraction of its parent hadron. The pdf's are determined empirically from experimental data [2, 3].

In hadron collisions, the highly energetic scattered partons radiate additional partons analogous to the radiation of a moving electric charge [4]. Because color charge is confined, the radiation from the scattered partons begins to form final-state particles through the process of "hadronization." Often, the radiated partons will form clusters of energy resulting in collimated sprays of final-state particles. These

particle clusters are defined as "jets." Jets are typically conelike, emanating from the interaction point.

QCD has been successful in calculating the rate (cross-section) of jet production in high energy (large momentum transfer) regimes. Jet production in hadron-hadron collisions can be separated into three stages: the intial state, the hard parton interaction, and the final state. These three stages can be factorized into five distinct calculational conveniences:

- The initial-state parton configuration: These are represented by the nonperturbative parton distribution functions.
- The initial-state parton radiation: Also called "parton showering," this process is calculated perturbatively down to energies where perturbative calculations begin to diverge.
- The hard parton-parton interaction: This can be calculated perturbatively to a fixed order of expansion in α_s
- The final-state parton radiation: This process is also called "parton showering."
- Hadronization: This process is nonperturbative and is empirically derived.

Perturbative QCD gives predictions for the hard interaction. The initial and final states are nonperturbative and must be calculated empirically from data. In factorizing each subprocess, separate calculations are performed only in the regimes where they are applicable. Therefore, this factorization scheme allows for the calculation of jet events that would otherwise not be calculable.

1.2 Invariant Phase Space

In describing the physics of hadron-hadron collisions, a Lorentz invariant phase space (coordinate system) is used consisting of three variables: azimuthal angle ϕ, rapidity y (or pseudorapidity η), and transverse momentum $p_T(E_T)$. The azimuthal angle is in the plane perpendicular to the initial hadron direction, or collision axis (z-axis). The rapidity is a measure of a particle's longitudinal fractional momentum (along the z-axis) and relates to the scattering angle. Pseudorapidity is a relativistic approximation of rapidity and is used often experimentally. The transverse momentum represents a particle's momentum perpendicular to the collision axis. These variables combine into an invariant phase space,

$$\frac{d^3p}{E} = p_T \, dp_T \, dy \, d\phi,$$

which under a longitudinal Lorentz boost undergo the transformations:

$$p_T \rightarrow p_T$$

$$\phi \rightarrow \phi$$

$$y \rightarrow y + constant.$$

Under a longitudinal Lorentz boost, the ϕ and p_T of the final-state objects and the $\Delta\eta$ separation of the jets remains unchanged. Commonly, a final state picture of what a detector finds after a collision is mapped into a two-dimensional η-ϕ space. The coordinate system used in this analysis is described in more detail in chapter 2.

1.3 Color Flow and Particle Multiplicity

In a typical QCD event, color is exchanged by the initial partons. The resulting hadronization from the "flow," or exchange, of color between the partons results in

particle production that is on average uniformly distributed in the event. When the final-state partons hadronize into two jets, color exchange results in particle production in the rapidity (η) region between the jets. Figure 1.2 shows a Feynman diagram of a color exchange event and a depiction of the final-state particles produced in η and ϕ.

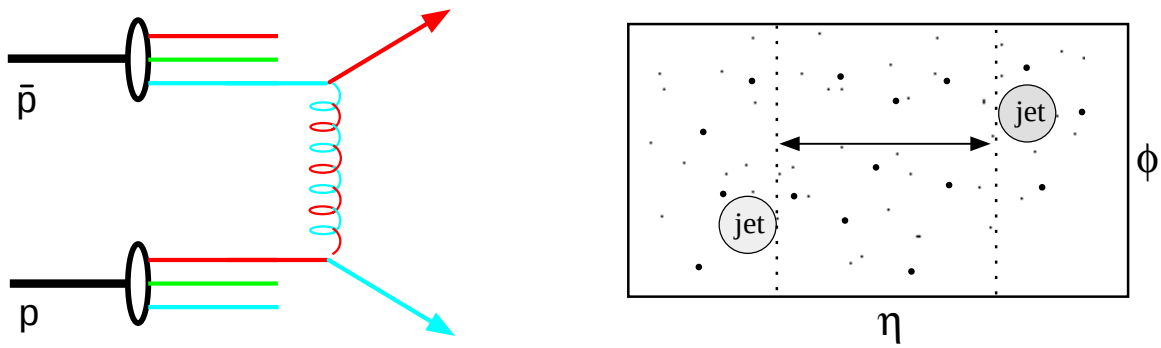

Figure 1.2. Feynman diagram of color exchange and the resulting particle production in η and ϕ.

In contrast to typical QCD events, this analysis studies a class of events arising from strong interactions but not well described by current perturbative QCD theories. The mediator of these events is a strongly-interacting color-singlet object that carries no net color charge. In events where a color-singlet is exchanged, no color is flowing between the scattered partons. As a result, particle production is suppressed in regions of the event. When the final-state partons hadronize into two jets, a minimal number of final-state particles is produced in the rapidity region between the jets. A region of rapidity containing no final-state particles is defined as a *rapidity gap*. Figure 1.3 shows a Feynman diagram of a color-singlet event and a depiction of the final-state particles produced in η and ϕ. Since there is no color flow between

the scattered partons, particle production is suppressed in the η region between the jets. Nonetheless, color still flows between the final-state partons and their respective proton "remnants" resulting in particle production in the η regions between the jets and the remnants.

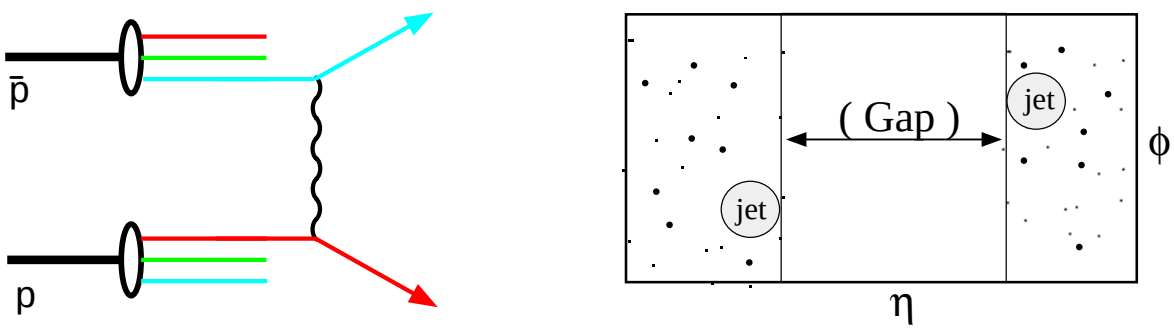

Figure 1.3. Feynman diagram of color-singlet exchange and the resulting rapidity gap and particle production in η and ϕ.

Since the clear difference between generic QCD events and those mediated by a color singlet is the presence of rapidity gaps, rapidity gaps are used as a signature for color-singlet exchange events. It is possible for rapidity gaps to arise in QCD from statistical fluctuations; however, as the rapidity separation of the two leading jets increases the probability for QCD to produce gaps decreases. Therefore, to measure the rate of color-singlet exchange in hadron interactions, events with large rapidity separation between the jets are selected. In these events, distinguishing the presence of a rapidity gap is reduced to counting the number of particles (i.e., particle multiplicity distribution) in the η-region between the jets.

Figure 1.4 shows a cartoon of the multiplicity distributions for color-singlet events and color exchange events. Counting the number of particles between the

two leading jets of a color-singlet exchange event yields a distribution that has a mean close to zero. Ideally, a color-singlet exchange event would not produce any particles between the jets. In reality, hadronization and detector effects (calorimeter showering and noise) may result in a low number of particles being measured. For color exchange events, the multiplicity distribution is a smooth curve with a large mean. In measuring the rate of color-singlet exchange, the color-singlet signal is observed as a low multiplicity excess over a smooth color exchange background. To achieve maximum separation of the signal and the background, detection efficiency should be high. This is obtained by using a low energy threshold for particle detection (increasing the efficiency for observing particles). In addition, requiring that the leading jets be widely separated in η tends to increase the mean of the color exchange multiplicity, decreasing the amount of background under the low multiplicity signal.

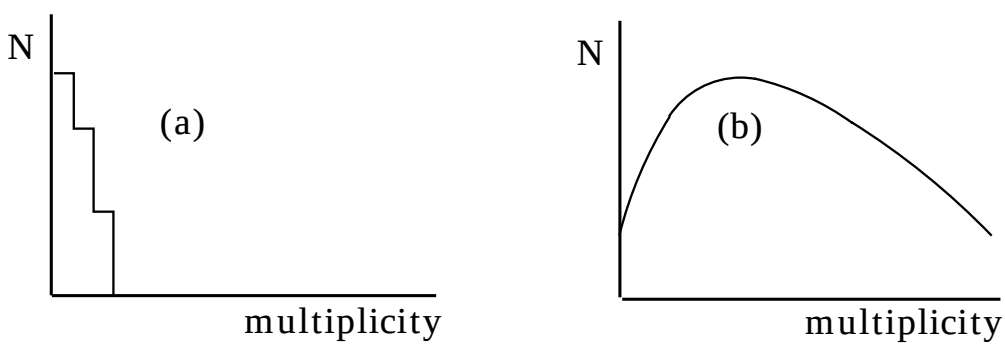

Figure 1.4. Depiction of particle multiplicity distributions between the two leading E_T jets for (a) color-singlet exchange and (b) color exchange.

1.4 Color-Singlet Exchange Fraction

In this analysis, the quantity that is measured experimentally is the fraction of color-singlet exchange events observed via rapidity gaps. The color-singlet fraction, or

rapidity gap fraction, is the ratio of the color-singlet cross-section and the total "dijet" (at least two jets) cross-section multiplied by the overall probability of a rapidity gap to "survive" contamination from spectator interactions. The observable rapidity gap fraction is then

$$f_{obs} = S \cdot \frac{\sigma_{gap}}{\sigma_{dijet}} \tag{1.1}$$

where S is the survival probability.

1.4.1 Survival Probability

Not all of the color-singlet exchange events will be observed experimentally because the rapidity gaps for some events may be contaminated by particles not produced by the hard interaction. In addition to the hard parton-parton interaction, hard scattering events have a large probability for parton-parton spectator interactions. These are soft interactions between partons in the proton and antiproton that are not involved in the hard scatter. Spectator interactions can introduce particles into the gap region, "spoiling" the rapidity gap. The probability that spectator interactions do not contaminate the region between the jets is called the survival probability.

Survival probability is calculated by considering the overlap of the proton and anti-proton in phase space. It was first estimated to be approximately 5 to 10% [5] using the form,

$$|S(B)|^2 = e^{-\nu\chi(B)} \tag{1.2}$$

where B is the impact parameter between the proton and anti-proton, $\chi(B)$ is a convolution of parton densities, and ν is a constant. More rigorous calculations using a variety of eikonal models yield a larger range of possible values (5-30%)[6]. Recent

results indicate that the survival probability could differ by a factor of 2 for the two center-of-mass energies used in this analysis [7].

1.5 Color-Singlet Models

This analysis will present results on the measurement of the color-singlet fraction as a function of dijet transverse energy (E_T), dijet pseudorapidity separation ($\Delta\eta$), and the proton-antiproton center-of-mass energy($\sqrt{s}$). Measuring the color-singlet fraction as a function of these variables probes the color-singlet dynamics and its coupling to quarks and gluons.

Several theories currently exist to explain the dynamics of color-singlet processes. One aim of the experimental results presented in this thesis in combination with those presented in references [8, 9, 10] is to aid in the discrimination between the theories. The most fundamental question regarding the color-singlet process is still unanswered: Is it mediated by a strongly-interacting color-singlet object, historically called the *pomeron*, is it a non-perturbative QCD effect due to the cancellation of color flow, or is it a signature for new physics?

1.5.1 Two-Gluon and BFKL

Although standard QCD (next-to-leading order (NLO) calculations and parton shower Monte Carlos) cannot account for the existence of hard color-singlet exchange, higher-order QCD processes may explain this phenomenon [5, 11, 12, 13, 14]. The exchange of two perturbative gluons in a color-singlet state was originally proposed by Bjorken as a simple mechanism to produce rapidity gaps between jets with a predicted color-singlet fraction on the order of 1-5% depending on the initial-state partons [5].

In the two-gluon model, each scattering process (qq, qg, or gg) has different color factors contributing to its cross-section. The color factors are contained in the fractional weighting of the parton distribution functions in the QCD color-singlet and color-octet states. Color-octet exchange is simply represented by the exchange of one gluon. The color singlet, however, has an additional color factor to account for the vertices of the second gluon. The relative weighting of singlet to octet is given by,

$$w(x) = \frac{G(x,Q^2) + \left(\frac{4}{9}\right)^2 \sum_f Q_f(x,Q^2)}{G(x,Q^2) + \frac{4}{9}\sum_f Q_f(x,Q^2)}, \tag{1.3}$$

where $G(x,Q^2)$ and $Q_f(x,Q^2)$ are parton distribution functions in terms of x (parton momentum fraction) and Q (the scale of the hard scatter).

The weight, w^2 can be interpreted as the suppression of color-singlet exchange compared to color-octet exchange given a particular x value. Two-gluon exchange via gg scattering, $w^2 = 1$, has a larger color factor, and therefore a larger cross-section, than that for qq scattering, $w^2 = (4/9)^2 \cong 0.2$. From these color factors, pure qq scattering is expected to have a rapidity gap fraction as small as 20% of the gg scattering rapidity gap fraction:

$$f(gg) = \frac{9}{4} f(qg) = \left(\frac{9}{4}\right)^2 f(qq) \tag{1.4}$$

$$\frac{f(qq)}{f(gg)} = \left(\frac{4}{9}\right)^2 \cong 0.2. \tag{1.5}$$

Since the two-gluon singlet couples more strongly to gluons by a $9/4$ color factor compared to single gluon exchange, the observed color-singlet fraction is expected to decrease with increasing initial-state quark processes (i.e., increasing parton x). The color-singlet fraction is expected to fall with increasing dijet E_T, increasing dijet $\Delta\eta$ separation, and decreasing $\sqrt{s}$.

This simple two-gluon picture has been expanded to include certain dynamical effects using a leading-log BFKL approximation to two-gluon exchange [12]. The probability, P, that an elastic collision produces a rapidity gap containing no parton radiation with E_T larger than μ between the jets can be expressed in terms of the weighting functions as,

$$P(\mu; x_p, x_{\bar{p}}) = w(x_p)w(x_{\bar{p}})\frac{\hat{\sigma}^{sing}}{\hat{\sigma}_{tot}} + \frac{\hat{\sigma}^{oct}_{gap}(\mu)}{\hat{\sigma}_{tot}} \tag{1.6}$$

where $\hat{\sigma}^{sing}$ is the cross-section for two-gluon color-singlet BFKL Pomeron [15] exchange, $\hat{\sigma}^{oct}_{gap}(\mu)$ is the cross section for color-octet exchange containing no parton radiation with transverse momentum greater than μ between the jets, and $\hat{\sigma}_{tot}$ is the inclusive jet cross section. Including BFKL effects leads to a rapidly decreasing color singlet fraction with increasing dijet E_T and a rising color-singlet fraction at large dijet $\Delta\eta$.

1.5.2 Soft Color Rearrangement

The soft color rearrangement model [14] asserts that the formation of a rapidity gap is a random process occurring after the hard scattering. In this model, color flow (via the exchange of a gluon or quark) can be cancelled by the exchange of nonperturbative soft gluons, leading to an "effective" colorless exchange. Figure 1.5 depicts how color can rearrange itself to produce a rapidity gap. In the figure, the bold lines indicate the rearrangement of the color strings. The "$\bar{3}$-3" states form effective color-singlets, resulting in a rapidity gap between the jets.

Since initial-state quarks have fewer possible color combinations than initial-state gluons, it is more likely that a cancellation of the color charge would occur for qq scattering. In contrast to the two-gluon model, this model predicts a color-singlet fraction that increases with increasing initial-state quark processes.

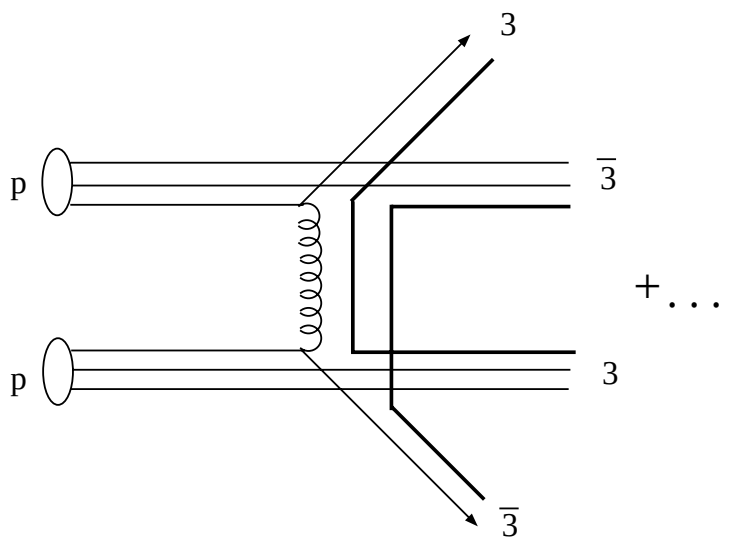

Figure 1.5. Rapidity gap formation in a pp collision via an effective color-singlet produced by the rearrangement of soft color strings (bold lines). The "$\bar{3}$-3" states form effective color-singlets.

1.5.3 An Alternative Model

An alternative to the QCD-based models, the exchange of a hard U(1) gauge boson that couples only to baryon number (quarks), has been proposed to explain the observed rapidity gap phenomena [16]. With an appropriate choice of the mass and coupling constant, a color-singlet fraction of 1% can be obtained. Since the boson couples only to quarks, the color-singlet fraction is predicted to increase with increasing initial-state quark content. Dynamics of the gauge boson predict a color-singlet fraction that increases with dijet E_T more rapidly than from parton distribution functions alone.

1.6 Previous Measurements

The study of rapidity gap physics at DØ was inspired by Bjorken's two-gluon model for the Pomeron. Data from DØś first collider run (1992-93) was used to place an upper limit of 1.1% on the rapidity gap fraction for events with a rapidity separation of $\Delta\eta > 4.4$ [17, 18].

Succeeding measurements used fitting techniques to the particle multiplicity distributions to extract the fraction of color-singlet exchange events. In DØś second rapidity gap publication, a measured color-singlet fraction of

$$f_s = (1.07 \pm 0.10(stat)^{+0.25}_{-0.13}(syst))\%$$

was quoted [19]. DØ used the measured color-singlet fraction to exclude electroweak exchange with a color-exchange background as the source of the excess. The probability that the observed color-singlet fraction was caused by electroweak exchange was determined to be less than 10^{-10}. The other collider experiment at Fermilab, CDF, also used fitting techniques to measure the color-singlet fraction of [20]

$$f_s = (0.85 \pm 0.12(stat)^{+0.24}_{-0.12}(syst))\%.$$

These measurements combined to provide the first evidence for a strongly-interacting color-singlet.

Recently, DØ has measured the color-singlet fraction as a function of dijet E_T and dijet $\Delta\eta$ separation at high E_T [8]. These results along with the results in this thesis, and results from a Monte Carlo comparison will soon be published.

CHAPTER 2

THE DØ EXPERIMENT

The DØ experiment, located at Fermi National Accelerator Laboratory (Fermilab) in Batavia, IL, was proposed to study proton-antiproton collisions at a center-of-mass energy 1.8 TeV. The DØ detector [21] is a complex apparatus designed primarily to investigate large mass and high transverse momentum (p_T) phenomena in hadronic collisions. These include the observation and measurement of the top quark, precision measurements of W and Z bosons, production and study of b-quark hadrons, tests of perturbative QCD, and searches for new phenomena beyond the standard model.

2.1 The Fermilab Tevatron $p\bar{p}$ Collider

The Fermilab Tevatron (figure 2.1) accelerates protons and antiprotons to energies of 900 GeV providing a center-of-mass colliding energy of 1.8 TeV. Currently the world's highest energy particle accelerator, the Tevatron reaches such energies in several stages using five individual accelerators. This section summarizes the Fermilab accelerator complex and relies heavily on reference [22].

The process begins by accelerating negative hydrogen ions to 750 KeV using an electrostatic field produced by a Cockcroft-Walton generator. The accelerated ions then reach 400 MeV in a linear accelerator. The ion beam is passed through a thin carbon target, stripping off the electrons. The resulting proton beam is accelerated to 8 GeV in the Booster Ring, and then to 120 GeV in the Main Ring. The Main Ring accelerator, with a circumference of 3.7 miles, functions as the injector to the

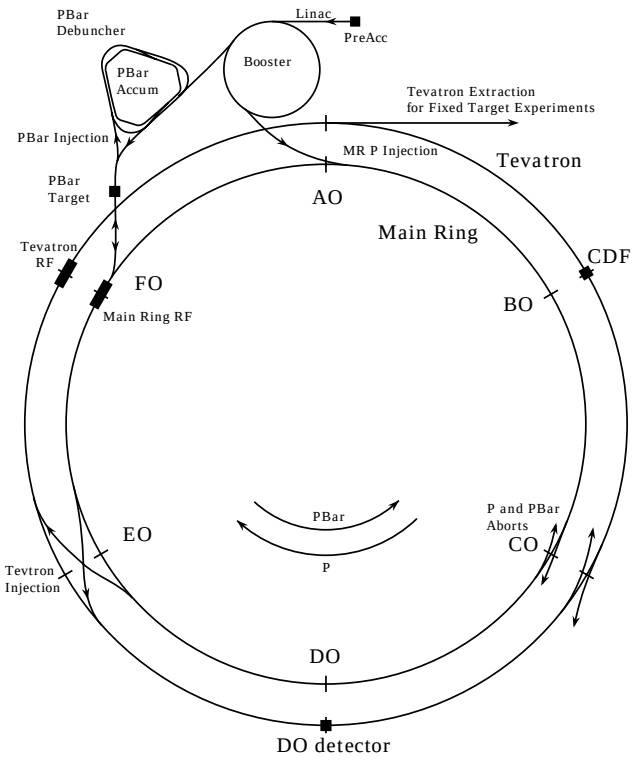

Figure 2.1. Overview of the Fermilab accelerator complex with the DØ and CDF detectors.

Tevatron as well as a proton source for antiproton production. Antiprotons are created by focusing the 120 GeV proton beam into a copper/nickel target. Roughly, one 8 GeV antiproton is produced for every 10^5 incident protons. The antiprotons are corrected for large angular dispersion, focused into a manageable beam, and then sent to the Accumulator. Accumulation continues for several hours until there are on the order of 10^{11} antiprotons.

Protons and antiprotons, in a structure of six bunches, are injected into the Main Ring in opposite directions and accelerated to 150 GeV before final injection into the Tevatron. The Tevatron uses superconducting magnets, producing a magnetic field

of up to 4 Tesla, to keep the 900 GeV protons and antiprotons in a circular orbit. Electrostatic separators prevent the proton and antiproton beams from colliding anywhere except in the specified interaction regions. At the two interaction sites (at the DØ and CDF detectors), quadrupole magnets focus the beams into collision. Beam crossings occur every 3.5 μs. A collider run can continue for up to 20 hours, during which antiproton accumulation continues for the next collider run.

The instantaneous luminosity of the collisions, or the proton-antiproton flux as compared to the rate of $p\bar{p}$ collisions, is a function of the bunch density and crossing time. During a run, the luminosity decays exponentially from its initial value. Over the course of DØ's first running period (1992-96), luminosity ranged from values of 0.2-20 $\times$ 10^{30} $cm^{-2}s^{-1}$.

2.2 Coordinate Systems

As many as four coordinate systems are used in describing the DØ detector: Cartesian (x, y, z), cylindrical (r, ϕ, z), spherical (r, ϕ, θ), and a subset of the spherical coordinate system (η, ϕ). These coordinate systems originate at the detector's geometric center and are shown in figure 2.2. The positive z-axis is aligned along the proton beam direction. The positive y-axis points vertically upward. Thus, the positive x-axis points radially inward. The angles ϕ and θ are the azimuthal and polar angles respectively.

The (η, ϕ) system is an extension of the spherical coordinate system and involves the rapidity variable, y. Rapidity is defined as

$$y = \frac{1}{2} \ln \frac{E + p_z}{E - p_z} \tag{2.1}$$

where E is the total energy and p_z is the longitudinal (z) component of the momentum

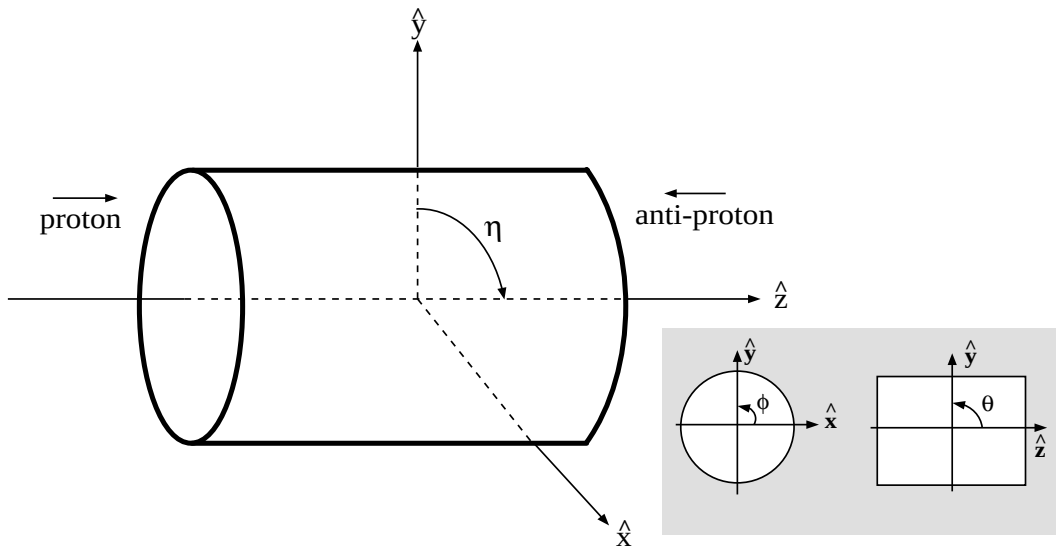

Figure 2.2. Coordinate systems. The coordinates z (beamline direction), η (rapidity), and ϕ (azimuthal angle).

of the particle. The rapidity differential is a Lorentz invariant quantity, making it a useful variable for describing particle distributions since a longitudinal boost of the system has no affect on the shape of the rapidity distribution. At Tevatron energies, the particle momentum is much larger than its mass, such that $E \simeq p$ and

$$y \simeq \frac{1}{2} \ln \frac{1 + E_z/E}{1 - E_z/E}. \tag{2.2}$$

Using the definition $\cos\theta = E_z/E$, the rapidity becomes

$$y \simeq \frac{1}{2} \ln \frac{\cos^2\theta/2}{\sin^2\theta/2}. \tag{2.3}$$

The pseudo-rapidity variable,

$$\eta_d \equiv -\ln \tan \frac{\theta}{2} \tag{2.4}$$

(η = y for massless particles) is typically used along with the azimuthal angle ϕ to measure and describe particle distributions in the detector. Centered in the detector ($z = 0$), (η_d, ϕ_d) represent the "detector coordinates." However, event vertices are typically not centered in the detector. Using the displaced vertex as the origin of the coordinate system, (η, ϕ) are defined as the "physics coordinates."

Particle and jet energy and momentum are most commonly described transversely to the beamline, and are denoted as E_T and p_T respectively. Using the polar angle, θ, the transverse energy can be defined as

$$E_T = E \sin\theta \tag{2.5}$$

and similarly for p_T.

2.3 The DØ Detector

Weighing in at 5500 tons, the DØ detector was optimally constructed for the identification and measurement of electrons, muons, high p_T jets, and missing transverse energy ($\not{E}_T$) which aids in neutrino identification.

A cutaway view of the detector is shown in figure 2.3. It is approximately 13 meters in height and 20 meters in length. The detector can be broadly divided into three detector systems: the central tracking system, the calorimeter, and the muon system. In the following descriptions, all detectors will be briefly reviewed and a more detailed discussion will be given for the primary detectors used in this analysis: the Central Drift Chamber, the Electromagnetic Calorimeter, and the Level Ø scintillating counters.

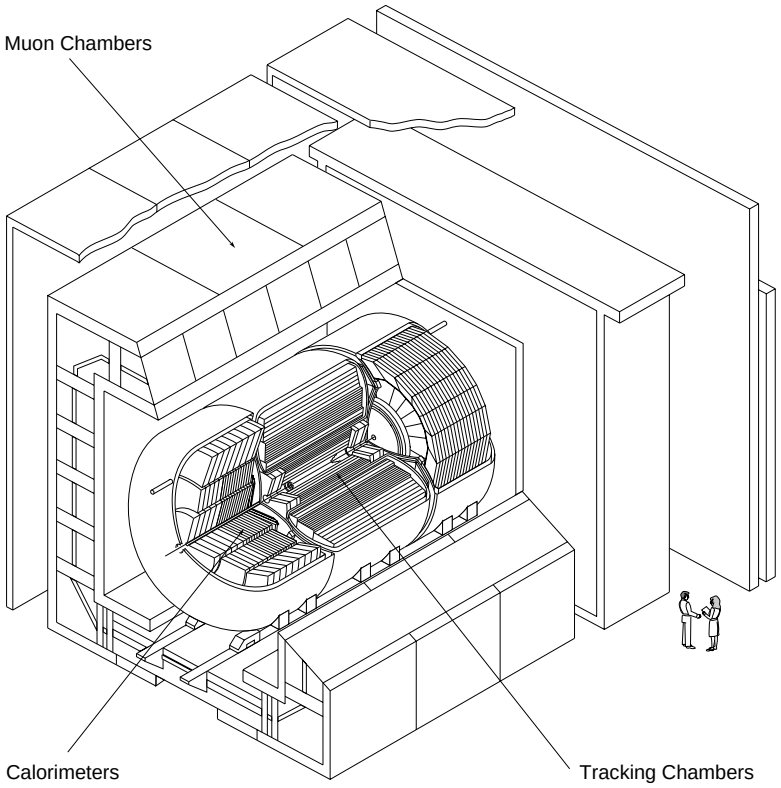

Figure 2.3. An overview of the DØ detector.

2.4 The Central Tracking System

At the center of the DØ detector lies the Central Tracking System. Consisting of four detector subsystems – the Vertex Drift Chamber (VTX), the Transition Radiation Detector (TRD), the Central Drift Chamber (CDC), and two Forward Drift Chambers (FDC) – the tracking system is positioned symmetrically around the beamline with an inner radius of 3.7 cm and an outer radius of 78 cm [21]. Figure 2.4 depicts a cross sectional view of the tracking subsystems.

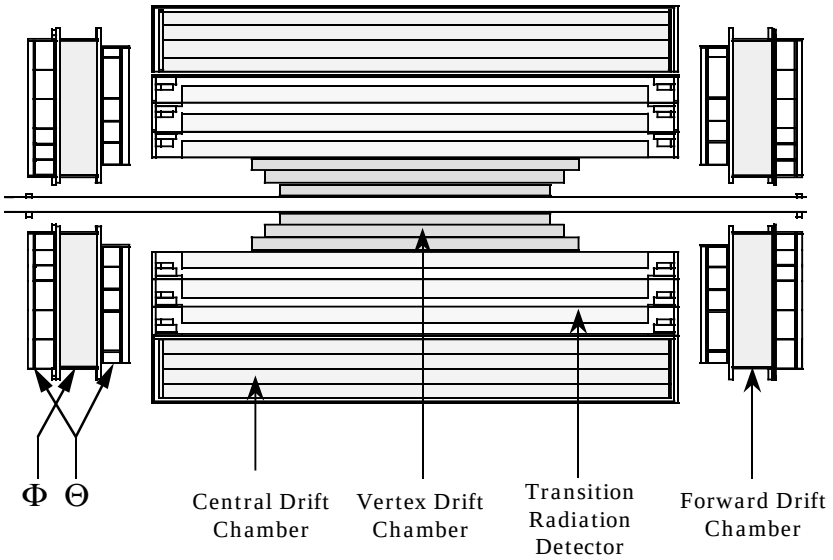

Figure 2.4. Components of the central tracking system.

The VTX, CDC, and FDC all use high electric fields inside ionizable gas media to measure charged particle trajectories. High-energy charged particles from the collision ionize the gas as they travel through each chamber. Drift times of the ionization electrons to an anode wire are used to measure the spatial position of the original ionizing particle. By combining timing signals from each of these detectors, particle track trajectories (r-ϕ positions) can be reconstructed. Since DØ lacks a central magnetic field, the reconstructed tracks are straight paths that provide no information about particle momentum or charge.

The VTX is the innermost tracking chamber and consists of three concentric layers of drift chambers designed to accurately measure the longitudinal position of the event vertex. The VTX spans a pseudorapidity range of $|\eta| < 2$. The resolution of the r-ϕ position is about 60 μm. The resolution of the z position is about 1.5 cm.

The transition radiation detector (TRD) is used to discriminate between low-mass objects (such as electrons) and higher-mass objects (pions and other hadrons). The detector consists of several layers of different dielectric media. Particles passing through the detector produce radiation at the boundaries of each of these dielectric layers that is inversely proportional to the particle's mass. In other words, low mass particles can be distinguished from high mass particles because they produce more radiation in the TRD.

The CDC surrounds the VTX and TRD and measures charged tracks within a pseudorapidity range of $|\eta| < 1.2$. It consists of four concentric layers of drift chamber modules, with each layer containing 32 azimuthal modules. The resolution of the r-ϕ position is about 180 μm, and the resolution of the z position is about 3 mm.

The FDC is positioned on each end of the central tracking detectors and covers a pseudorapidity range of $1.0 < |\eta| < 3.2$. Each FCD consists of three layers of drift chamber modules and provides an r-ϕ resolution of 200 μm and a z resolution of 4 mm.

2.5 The Calorimeter

The DØ calorimeter is designed to measure the energies of particles produced in hadronic collisions, providing kinematic information for electrons, photons, jets, and neutrinos. Calorimeter shower shapes provide additional information that is useful in the identification of electrons, photons, jets, and muons. A cutaway view of the calorimeter is shown in figure 2.5.

As a sampling calorimeter, the DØ calorimeter uses a series of measurement samples of particle shower energies to infer the total energy of the particle. The

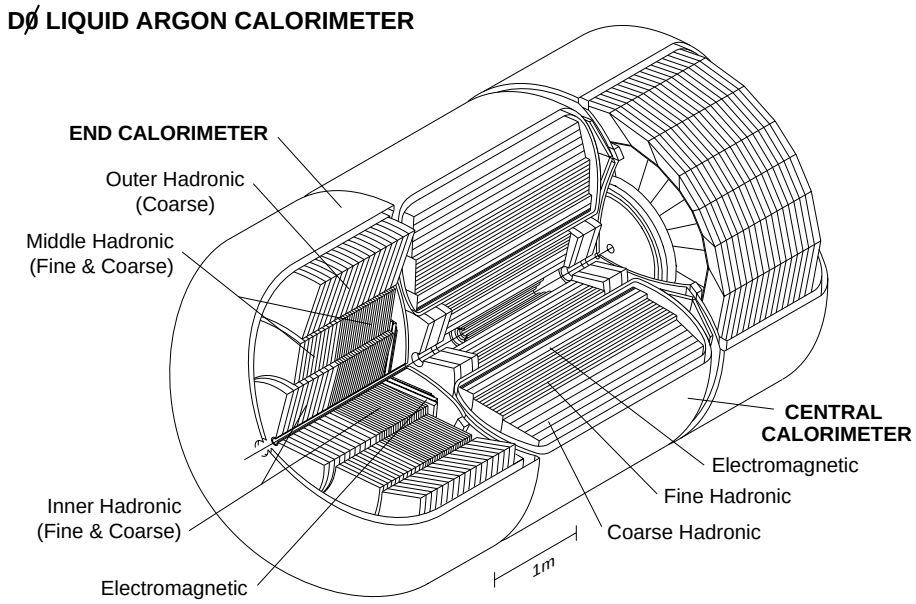

Figure 2.5. The DØ calorimeters consist of three individual cryostats (one central and two endcaps). The calorimeter subsystems are also shown.

calorimeter is constructed with many layers of dense absorbing material alternating with an ionizing medium. Particles traversing the calorimeter lose energy in the dense absorbing layers (typically depleted uranium), and a fraction of their remaining energy is measured in the ionizing medium (liquid argon). When passing through the absorber, a particle will interact with the uranium to produce low-energy secondary particles in a process called *showering*. The shower particles then ionize the liquid argon, and the energy fraction and location, in (η, ϕ) space, of the shower are measured.

High energy electrons and photons mostly interact with the absorbing material in a series of complementary processes: pair production and bremsstrahlung. With each interaction, the particle multiplicity increases and the average energy per particle

decreases. These showers are called *electromagnetic*, or EM, showers. Because the shower multiplicity (and energy sharing among secondaries) develops exponentially, the shower depth depends logarithmically on the primary energy. The likelihood that an electromagnetic particle survives a distance d without initiating a shower falls exponentially, given by

$$E(d) = E_0 e^{-\frac{d}{X_0}}, \tag{2.6}$$

where E_0 is the intial particle energy, and X_0 is the *radiation length* of the material. For Uranium, $X_0 \approx 3.2$ mm.

Unlike electromagnetic particles, high-energy hadrons interact with the uranium nuclei in strong interaction inelastic collisions producing secondary particles which also interact via inelastic collisions. This type of shower is denoted *hadronic* and develops over larger distances than an electromagnetic shower. The likelihood that a hadron survives a distance d without initiating a shower is also given by equation 2.6 where X_0 is replaced by λ_I, the *nuclear absorption length* of the material. For uranium, $\lambda_I \approx 10.5$ cm.

Since EM showers develop over much shorter distances than hadronic showers, the first several layers of the calorimeter are very closely spaced and are designed to accurately measure energies of EM particles. The outer layers of the calorimeter have a larger spacing useful for the measurement of hadronic energy. The hadronic section has two subsections: a fine hadronic (FH) section providing good hadronic shower energy resolution, and a coarse hadronic (CH) section used primarily for the containment of the highest energy showers.

The cell layer structure of the calorimeter is seen in figure 2.6. The layers are aligned in towers that project back towards the interaction region (the lower left-hand corner of the diagram). The cell layer sizes are determined by this geometry and by

the shower depth. EM layers are approximately 1-2 cm wide, and hadronic layers are approximately 10 cm wide. Typically, each calorimeter layer measures 0.1 units of η by 0.1 radians in ϕ. Therefore, each semi-projective tower also measures 0.1×0.1in (η, ϕ) space.

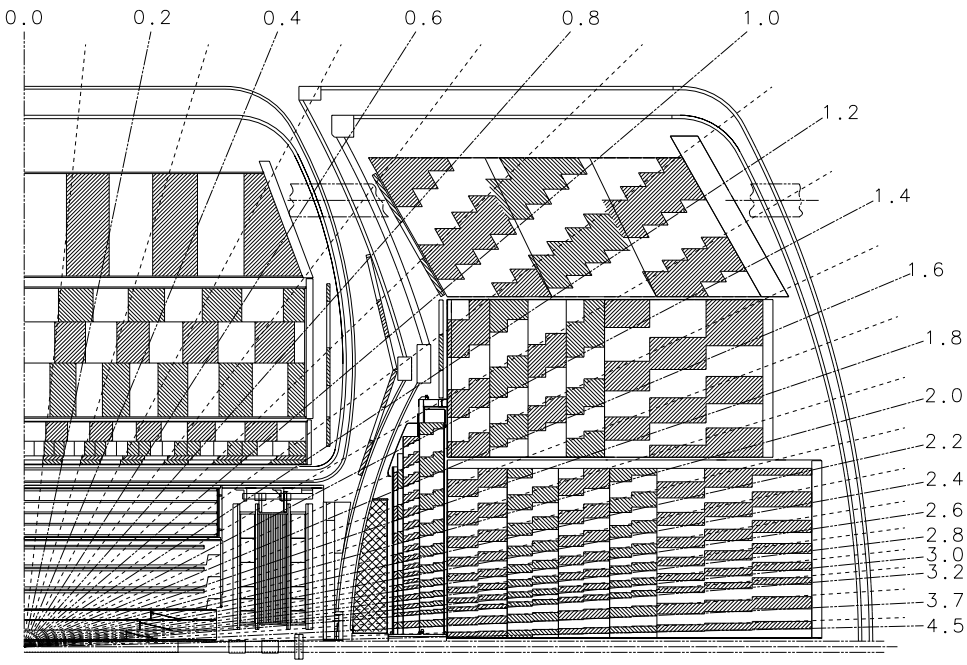

Figure 2.6. Side view of one-fourth of the calorimeter, showing projective cell structure for successive layers.

The liquid argon in the calorimeter is kept at a temperature of 78 K necessitating a stainless steel cryostat housing. The calorimeter is structurally divided into three independent cryostats to facilitate access to the tracking detectors. There is one Central Calorimeter (CC) cryostat located between two Endcap Calorimeter (EC) cryostats.

2.5.1 Central Calorimeter

The Central Calorimeter (CC) is cylindrically shaped, and provides coverage to $|\eta| \leq 1.0$. The readout layers are stacked in r. The first four layers of the CC (counting from proximity to the beam pipe) provide EM measurement at depths of 2, 4, 11, and 21 X_0 interaction lengths, which together comprise about 0.76 nuclear absorption lengths. The first, second, and fourth layers have cell segmentation of 0.1×0.1 in η-ϕ space. Since maximum shower development occurs in the third layer, the cell segmentation is increased to 0.05×0.05 to provide a more precise measurement of the shower location and shape.

Beyond the EM layers are three Fine Hadronic (FH) layers at depths of 1.3, 1.0, and 0.9 nuclear absorption lengths. All three layers have cell segmentation of 0.1×0.1. After the FH is the Coarse Hadronic (CH) layer, providing one readout layer with a depth of 3.2 nuclear absorption lengths.

2.5.2 End Calorimeters

The Endcap Calorimeters (EC) lie on each side of the CC, extending coverage out to $|\eta| \leq 4.0$. The EM readout layers have thicknesses of 0.3, 2.6, 7.9, and 9.3 X_0, which together comprise about 0.75 nuclear absorption lengths. For $|\eta| \leq 2.6$, the cell segmentation is the same as for the CC. Beyond this point, however, the cell sizes become smaller than the EM shower size. Beyond $|\eta| \leq 2.6$, the segmentation of the third layer is decreased to 0.1×0.1. Beyond $|\eta| \leq 3.2$, the segmentation for all four layers is decreased to 0.2×0.2 and continues to decrease until reaching 0.4×0.4 at $|\eta| \leq 4.0$.

In the EC, there are three hadronic modules. Closest to the beam pipe is the inner hadronic module consisting of four fine hadronic (IFH) readout layers and one

coarse hadronic (ICH) readout layer. The middle hadronic module surrounds the inner module in ϕ and has four fine hadronic (MFH) layers and one coarse hadronic (MCH) layer. The outermost module in ϕ is the outer hadronic module (OH) and consists of three coarse hadronic layers. In the region $0.7 < |\eta| < 1.1$, the EM and FH calorimetry are in the central calorimeter, and the CH calorimetry is in the EC.

2.5.3 Intercryostat Detectors

Because of the structure and support system of the calorimeter cryostats, a gap in calorimeter coverage exists between the Central and End Calorimeters. The gaps approximately span $0.8 \leq |\eta| \leq 1.4$, resulting in partial instrumentation of the EM and FH sections. This partial coverage creates a lack of uniformity in the energy response and acceptance in this region. In particular, this region has a substantial amount of absorber material without energy sampling in the first interaction length. To supplement the coverage, the Intercryostat Detector (ICD) was installed. The ICD consists of scintillation counter arrays and is positioned on the inner EC cryostat walls to provide an energy sample in this region.

Additional coverage is gained by the Massless Gaps (MG). These detectors are read-out cells consisting of signal boards, without a sandwiched absorber, embedded in liquid argon and are positioned just inside both the CC and EC cryostat walls providing full coverage in ϕ.

2.5.4 Calibration

Before DØ reached the final stages of construction and assembly, the calorimeter design was fully tested and calibrated at the DØ test beam [23]. For example, one set of ECEM and ECIH modules was installed in the final detector after being calibrated in the test beam. Using monoenergetic beams of electrons and charged pions with

energies ranging from 2-150 GeV, studies indicated that calorimeter response is linear for electrons with energies greater than 10 GeV and for pions greater than 20 GeV. For low energy particles, the response is nonlinear, resulting in decreased particle detection efficiency and jet energy response. At low energies, noise degrades signal resolutions. But at higher energies, resolutions are dominated simply by calorimeter inhomogeneities and calibration errors. Calorimeter resolutions σ_ε have been measured to be about $15\% \cdot \sqrt{E}$ for electrons and $50\% \cdot \sqrt{E}$ for pions. The jet energy resolution was determined offline to be approximately $85\% \cdot \sqrt{E}$.

After DØ was fully installed, calibration continued every few days between collider runs. Sending pulsed signals through each preamp in the calorimeter, each read-out channel could be calibrated. The calibration data was used to find gain corrections for the preamps, and these corrections were stored in a database that was used to correct each calorimeter read-out channel during offline data reconstruction.

2.5.5 Noise

Noise can be created in the calorimeter by both the uranium and the electronics used. The noise distributions from these two sources can be distinguished. Resulting from beta decay in the uranium absorber plates, the uranium noise produces a Landau distribution with a long high-energy tail. In contrast, the electronics noise produces a symmetric Gaussian distribution.

During the running period, the noise distribution, or pedestal, in each calorimeter channel was measured almost every day during times when no beam was present in the Tevatron. By fitting the noise distribution of each channel with a Gaussian, the mean and width of the noise pedestal was determined. These values were used while taking data to suppress any channel if it was within 2σ of the pedestal value.

This procedure is called *zero suppression* and greatly reduces the number of channels recorded for each event.

The noise distributions produced in each section of the calorimeter (EM, FH, and CH) differ because of differences in the geometry of the read-out cells. Electronic noise and uranium noise are proportional to the area (capacitance) of the read-out cell and to the number of gaps in the cell. Therefore, smaller cells will have comparatively less noise. Typical noise widths found in the different calorimeter sections are given in table 2.1 [23]. Because cell sizes are smallest closest to the beam pipe, the EM section has the lowest noise level.

TABLE 2.1

TYPICAL CALORIMETER NOISE WIDTHS BY
CALORIMETER SECTION AND CRYOSTAT

Section	CC Pedestal Widths (MeV)	EC Pedestal Widths (MeV)
EM	10	10
FH	60	30
CH	75	55
ICD	8	15
MG	30	30

Noise and zero suppression have little effect of high-p_T objects like electrons and photons. However, they can have a large effect on low energy particle detection ($E <$ 1 GeV). The observation of low energy particles in the calorimeter can be hidden by fluctuations in noise. Clearly, the EM section of the calorimeter is most efficient for detecting low energy particles and is, therefore, the most important detector for this analysis.

2.6 Muon System

Muons are not found in this analysis, and so the Muon System of the DØ detector is only summarized for completeness. In the calorimeter, muons are detected as minimum ionizing particles but are not usually absorbed. Muons have fairly long lifetimes ($\sim 2.2\mu$s) such that they are unlikely to decay within the volume of the calorimeter. Muons are massive (106 MeV), restricting their ability to induce an electromagnetic shower. In addition, muons do not interact strongly and are unable to induce hadronic showers. For all of these reasons, a separate detector subsystem for measuring muons and their momenta encompasses the calorimeter.

The DØ muon system consists of several layers of proportional drift tubes (PDT's) on either side of iron toroidal magnets with a field strength of approximately 2 Tesla. The magnets are used to bend the muon tracks emerging from the calorimeter. The angular bend is used to calculate the muon momentum.

2.7 Triggering and Data Acquisition

At the DØ interaction region, $\bar{p}p$ crossings occur every 3.5 μs, and at typical luminosities, at least one collision will occur at almost every crossing. This rate far exceeds the ability of current technology for recording events. Fortunately, only a very small fraction of collisions actually produce interesting events. Therefore, DØ implements a series of triggering levels to filter and store the interesting events for analysis. There are three trigger levels, each increasingly more sophisticated, through which candidate events much pass specific requirements.

2.7.1 Level Ø

As the first level of the triggering system, the Level Ø is used primarily to flag inelastic collisions and to measure the luminosity at the collision site. An array of scintillation counters connected to photomultiplier tubes is mounted on the inner surface of each endcap cryostat. The arrays provide partial coverage in ϕ from $1.9 < |\eta| < 2.3$ and full coverage from $2.3 < |\eta| < 3.9$. Hits in both arrays (on either end of the interaction) coincident with a $\bar{p}p$ crossing suggest the existence of an inelastic collision. In addition, the timing difference between the two arrays can be used to determine the z-position of the interaction vertex and to determine whether multiple interactions occurred during one beam crossing. Events flagged as inelastic are then passed to the Level 1 trigger.

2.7.2 Level 1

As a framework of hardware logic circuits controlled by software, the Level 1 trigger uses coarsely but rapidly digitized information from the calorimeter and muon system to decide in under 3.5 μs whether an event meets specific energetic and topological requirements. For example, the calorimeter cell information is grouped into trigger towers of size 0.2×0.2 in η-ϕ space. A level 1 trigger might require one or more trigger towers above a certain energy for that event to be of interest. Furthermore, trigger towers might be required to have some minimum $|\eta|$ value, as is used in this analysis.

2.7.3 Level 2

The Level 2 trigger consists of software filters operating on fully digitized event data that were run on a farm of 48 VAXstation nodes working in parallel to reconstruct events passed from Level 1. Using information from all detector systems, the Level 2

filters try to reconstruct and identify specific event objects, like jet, electron, photon, and muon candidates. The filters can select events passing requirements on the E_T, η, ϕ, and number of objects. For this analysis, the Level 2 filters used an additional requirement to select events with two jets having a large separation in pseudorapidity.

A more detailed discussion of the triggers used in selecting the data for this analysis is presented in the next chapter.

2.8 Jet Reconstruction

After a hard partonic interaction, final state partons will carry a large momentum and a color charge. The partons undergo hadronization as a way to dispose of their color charge. The hadronization process produces collimated sprays of particles which can be grouped into energy clusters and defined as jets. At DØ, jets are identified using only the calorimeter, and in this analysis, their energy and location are determined by using an iterative cone algorithm. Ideally, the jet position and momentum reflect those of the original parton, but hadronization and particle showering introduce finite resolutions that depend on the details of the jet reconstruction algorithm.

2.8.1 Event Vertex

Since the E_T and η of a jet depend on the location of the event vertex, an accurate determination of the event vertex position is necessary to reconstruct the jets well. The vertex is determined by using tracking information from the CDC (or from the FDC when the CDC is unable to identify a vertex). For each event, every charged track is reconstructed and extrapolated to the beam axis constructing a distribution of track-beam intersections. A gaussian is fit to the distribution of

intersections, and the mean is the z vertex position for that event. It is possible that the track z positions may be clustered into more than one smooth distribution. When this occurs, each cluster is fit with a Gaussian and as many as three z vertices may be found. The vertex corresponding to the largest number of tracks is the primary vertex. If the FDC information is used to determine the vertex, only one will be found due to the high density of tracks in the forward region.

If no vertex is found using reconstructed tracks, the vertex position can be determined by using the timing difference between the two Level Ø scintillating arrays.

2.8.2 Jet Finding Algorithm

This analysis uses an iterative cone algorithm for finding jets in an event. The algorithm identifies energy clusters in the calorimeter through a several step process.

- **Seed Towers:** The first step in reconstructing jets is the identification of all calorimeter towers with $E_T > 1$ GeV. The geometric center of each cell and the reconstructed vertex position are used to construct towers as a vector sum of the energy in all layers at each calorimeter (η-ϕ) position. A list of these seed towers is made, storing the E_T and η-ϕ location of each tower.

- **Preclusters:** Preclusters are formed by summing the energy from a seed tower with the energies of neighboring towers within a radius $R = 0.3$ ($R = \sqrt{\Delta\eta^2 + \Delta\phi^2}$). Preclustering continues until all seed towers are grouped into a precluster. Isolated towers that cannot be grouped with others are considered their own precluster. The E_T, η, and ϕ of each precluster tower is used to determine the E_T-weighted center of each precluster as follows:

$$\begin{aligned} \eta_{cluster} &= \frac{\sum_i E_{T_i}\eta_i}{\sum_i E_{T_i}} \\ \phi_{cluster} &= \frac{\sum_i E_{T_i}\phi_i}{\sum_i E_{T_i}} \end{aligned} \tag{2.7}$$

- **Jets:** Using the η-ϕ position of each precluster as the initial jet cone center, the jet cone algorithm sums the E_T within a cone of radius R and determines a new jet η-ϕ centroid. A cone size of 0. 7 is used in this analysis. The process of finding a new jet centroid is iterated until a stable jet center is determined. Once the jet centroid is stable, the jet position is redetermined from

$$\begin{aligned} E_T &= \sqrt{E_x^2 + E_y^2} \\ \theta &= \tan^{-1}\frac{E_T}{E_z} \\ \eta &= -\ln\tan\frac{\theta}{2} \\ \phi &= \tan^{-1}\frac{E_x}{E_y} \end{aligned} \tag{2.8}$$

where,

$$\begin{aligned} E_x &= Esin(\theta)cos(\phi) \\ E_y &= Esin(\theta)sin(\phi) \\ E_z &= Ecos(\theta). \end{aligned} \tag{2.9}$$

As a final step, only jets with $E_T > 8$ GeV are retained. The final list of jets is then E_T-ordered; the leading jet refers to the highest E_T jet in the event.

- **Jet Splitting and Merging:** If the centers of two jet candidates are within $2R$ of each other, the algorithm must decide whether to divide the combined energy into two individual jets or merge the jet candidates into one. The decision to split or merge jet candidates is based on the E_T contained in the overlap region between them. If the E_T in the overlap region is greater than 50% of the lower E_T jet, the candidates are merged into one by summing all towers and

recalculating the new jet's centroid and E_T. If the E_T in the overlap region is less than 50% of the lower E_T jet, the candidates are split by assigning all towers in the overlap region to the nearest jet and recalculating the new centroid and E_T of the two jets.

2.8.3 Jet Energy Scale

The response of the calorimeter varies with pseudorapidity and is non-linear at particle energies below 10 GeV. Since jets typically contain many low energy particles, the measured jet energy is not proportional to the actual jet energy. Therefore, the calorimeter jet response, or jet energy scale, must be corrected to reflect the true jet energy. The jet energy is also corrected for calorimeter noise (both electronic and uranium noise), negative calorimeter signal pileup from the previous event, extraneous energy in the jet from the underlying event, and leakage out of the jet cone due to shower widths. The true jet energy is

$$E^{jet}_{particle} = \frac{E^{jet}_{measured} - O}{(1 - S)R_{had}}. \tag{2.10}$$

O is the offset factor which corrects for noise, pileup, and the underlying event. S is the calorimeter showering correction. R_{had} is the hadronic calorimeter response.

The determination of each of these correction factors is well documented in references [24] and [25].

CHAPTER 3

DATA SELECTION

The data used in this analysis was taken during the 1995–1996 Tevatron Collider run at both $\sqrt{s}$ = 1800 and 630 GeV. Two data sets are used for the 1800 GeV measurement: one sample has luminosities ranging from 2 to 5 $\times$ 10^{30} $cm^{-2}s^{-1}$, and one sample was taken during a special low luminosity running period with luminosities less than 1 $\times$ 10^{30} $cm^{-2}s^{-1}$.

3.1 Triggers

3.1.1 Level Ø and Level 1

Level Ø , the first of the three trigger levels, is used to determine the presence of an inelastic collision. Level Ø scintillation counters demand a coincidence of properly timed energy deposition in the far forward regions of both ends of the detector to signal that a potentially interesting event has just occurred. Events are vetoed during moments of main ring accelerator activity in order to reduce anomalous energy deposition in the calorimeter.

For all three data samples, the Level 1 trigger requires events to have two calorimeter trigger towers above an E_T threshold of 2 GeV and with $|\eta| > 1.0$. In obtaining the 1800 GeV data, a single interaction cut is included to reduce contamination from multiple interactions. The cut on single interactions uses particle detection rates from the Level Ø counters to make a calculation of the instantaneous luminosity.

The average number of interactions per crossing is given by,

$$\bar{n} = \mathcal{L}\,\tau\,\sigma_{\mathrm{L}\emptyset},$$

where $\mathcal{L}$ is the instantaneous luminosity, τ is the crossing time (3.5 μs), and $\sigma_{L\emptyset}$ is the cross section subtended by the Level Ø counters (46.7 mb). Using Poisson statistics, the expected number of single interactions is $\mathrm{P}(1) = e^{-\bar{n}}$. The online single interaction cut does not cut on all multiple interactions especially at higher luminosities, and so additional offline cuts are used[8].

3.1.2 Level 2 Filters

The Level 2 trigger requires events to have two jets with $E_T > 10$ or 12 GeV. The high luminosity 1800 GeV data set triggered on jets with $E_T > 12$ GeV. This requirement was lowered for the low luminosity 1800 GeV and the 630 GeV data sets in order to increase the number of events. The two trigger jets were also required to have $|\eta| > 1.6$. The high luminosity 1800 GeV data required a separation of the jet axes of $\Delta\eta > 4.0$. The low luminosity 1800 GeV data and the 630 GeV data required $\Delta\eta > 3.2$ in order to increase the number of events.

3.2 Offline Event Selection

3.2.1 Bad Run Removal

All runs which were determined to have problems with either the calorimeter or the Central Drift Chamber (CDC) are removed from the data sample. Also, two of the low luminosity runs were taken during a testing period of different proton bunch structures. These two runs were removed from the data set.

3.2.2 Calorimeter Noise Suppression

Noisy calorimeter towers in the central region may spoil a rapidity gap. Therefore, noisy towers in the electromagnetic calorimeter are not counted in measuring the calorimeter multiplicity between the jets. Noisy cells are identified by examining the occupancy of the EM calorimeter towers over intervals of several runs. Any tower that is greater than 3σ above the mean occupancy of the towers in a ring of ϕ at the same detector η is considered noisy. Figure 3.1 shows the EM tower occupancy for the high luminosity 1800 GeV data sample and a few noisy towers rising above the nominal value.

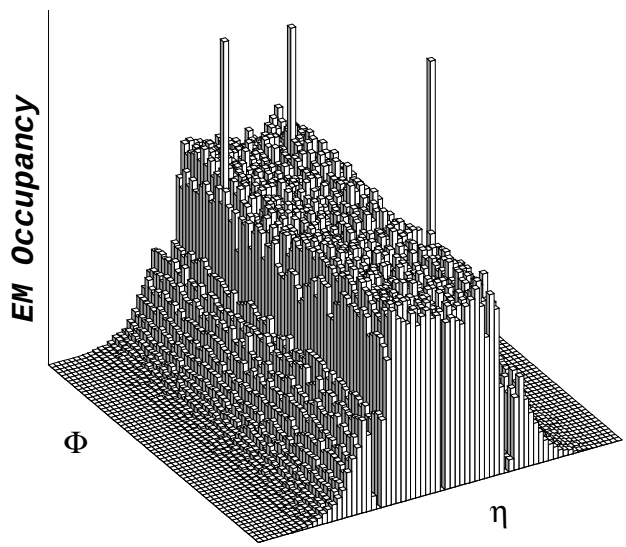

Figure 3.1. Electromagnetic calorimeter tower occupancy in η and ϕ showing a few noisy towers above the nominal value.

3.2.3 Jet Quality Cuts

Cuts on the jet quality have been studied and developed [26] to reduce contamination from spurious, or "fake," jets that have been misidentified either at the trigger

level or during reconstruction. If the two leading jets in an event do not pass the jet quality cuts, the event is discarded. The cuts are outlined as follows:

- **Electromagnetic Fraction:** The electromagnetic fraction (EMF) is the fraction of jet E_T deposited in the electromagnetic calorimeter. The EMF must be less than 95% for all jets and greater than 5% for jets with $|\eta| < 1$ or $|\eta| > 1.5$. This cut rejects approximately 95% [27] of fake jets resulting from noisy calorimeter cells, and is 99.9% [26] efficient for jets above $E_T = 30$ GeV.

- **Coarse Hadronic Fraction:** The fraction of energy deposited by a jet in the coarse hadronic calorimeter is required to be less than 40%. This cut removes about 95% of the spurious jets caused by main ring activity and about 99% of jets from noisy CH cells [28]. This cut is about 99% efficient for good jets above $E_T = 30$ GeV.

- **Hot Cell Fraction:** The hot cell fraction is defined as the ratio of the energy of the highest energy cell to the second highest energy cell in a jet. This fraction is required to be less than 10. The cut is very effective at removing jets that are caused by or contaminated with noisy calorimeter towers. The cut rejects 80% of fake jets from "hot" cells and retains 98% of real jets [26, 27].

3.2.4 Final Data Samples

In addition to the removal of bad runs and hot cells, and the requirement that jets pass the quality cuts above, other offline cuts are made to select the final data samples. Table 3.1 lists the offline cuts made and the resulting numbers of events.

A cut on multiple interactions is made by using a multiple interaction flag, MUL_INTF ≤ 1, and the number of vertices, N_VTX ≤ 1, rather than using the

TABLE 3.1

OFFLINE SELECTION CRITERIA

Cut	1800 GeV N_{events}	Percent Cut	630 GeV N_{events}	Percent Cut
Trigger	215,625	--	79,619	--
No. of Jets ≥ 2	212,703	1	76,366	4
Single Interaction	212,703	--	48,478	37
Vertex Position	136,723	36	39,822	18
Jet $E_T \geq 12$ GeV	126,869	7	25,591	36
$\Delta\eta \geq 4$	75,101	41	11,810	54
Jet Quality	69,640	7	10,430	12
$\mid \eta \mid \geq 1.9$	47,905	31	6,721	36

standard multiple interaction software tool, MI_RUN1, used in standard event reconstruction [29, 30]. This approach is necessary since the high luminosity 1800 GeV data was taken without reading forward tracking information. Most rapidity gap events have no central tracks, and the vertex position calculated using the CDC naturally fails. The vertex position for gap events, therefore, would otherwise be found using tracking information from the FDC. Since these high luminosity 1800 GeV events do not have FDC information available, the vertex position is calculated with Level Ø timing information. The multiple interaction tool, MI_RUN1, uses the tracking vertex in its calculations. Therefore, this tool cannot be used in this analysis. The low luminosity 1800 GeV data was used to study the effect of replacing the MI_RUN1 cut with cuts on MUL_INTF and the number of vertices and resulted in no effect on the measured color-singlet fraction. Since this data is at a fairly low luminosity, it is not surprising that the multiple interaction flag is effective at cutting out multiple

interactions.

Other cuts include a requirement that the primary vertex position, $|z| < 50$cm, to demand that events are centered in the detector. The two leading jets are required to have $|\eta| > 1.9$ to reduce out-of-cone contamination into the central region ($|\eta| < 1.0$) where the multiplicity is measured. The two leading jets must also have $E_T \geq 12$ GeV and $\Delta\eta \geq 4.0$.

Figure 3.2 shows the jet characteristics of the 630 GeV and 1800 GeV data samples after all cuts are applied. The two leading E_T jets are shown to be forward in η as demanded by the trigger. When they are present, third jets are required by the jet reconstruction algorithm to have $E_T > 8$ GeV. They have no trigger requirements and are central in η and have low E_T. All jets are uniform across ϕ. Figure 3.3 shows the event characteristics of the 1800 GeV and 630 GeV data samples after all cuts are applied. At lower center-of-mass energy, the jets are not as far forward and so the $\Delta\eta$ separation is reduced. The 630 GeV jets are also less boosted in η, have a smaller E_T difference, have fewer numbers of jets on average, and probe a higher parton x range. Both data samples are shown to have jets back-to-back in ϕ and events are centered in the detector.

Figures 3.4 and 3.5 show the topology of a typical rapidity gap event. Figure 3.4 is a detector event display and shows a side view of the tracking system with charged particle tracks, the reconstructed vertex position, and the calorimeter with energy deposition. Figure 3.5 shows the energy deposition in the calorimeter, which is represented by the height of the lego plot "towers."

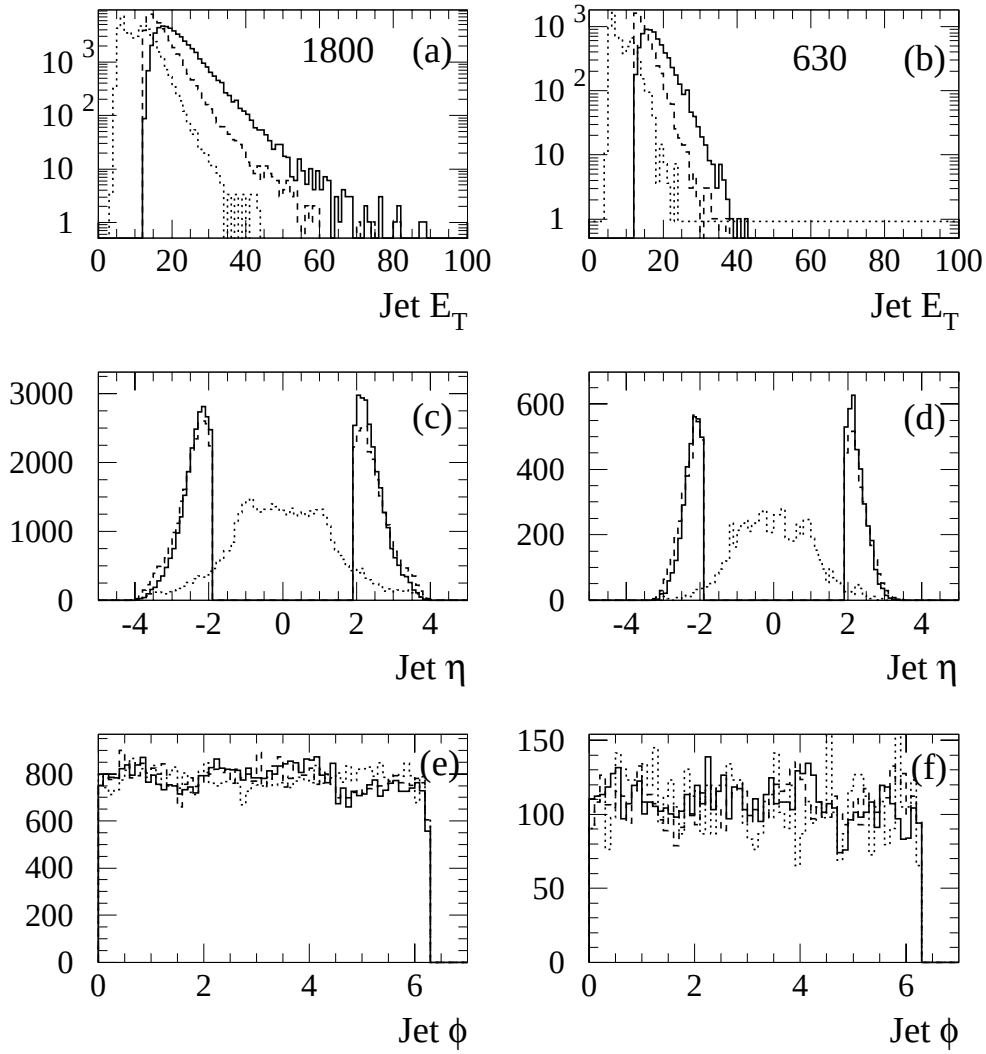

Figure 3.2. Jet characteristics of the 1800 GeV ((a),(c),(e)) and 630 GeV ((b),(d),(f)) data samples after all cuts are applied. The solid line is the leading E_T jet; dashed is second leading jet; dotted is third jet when present.

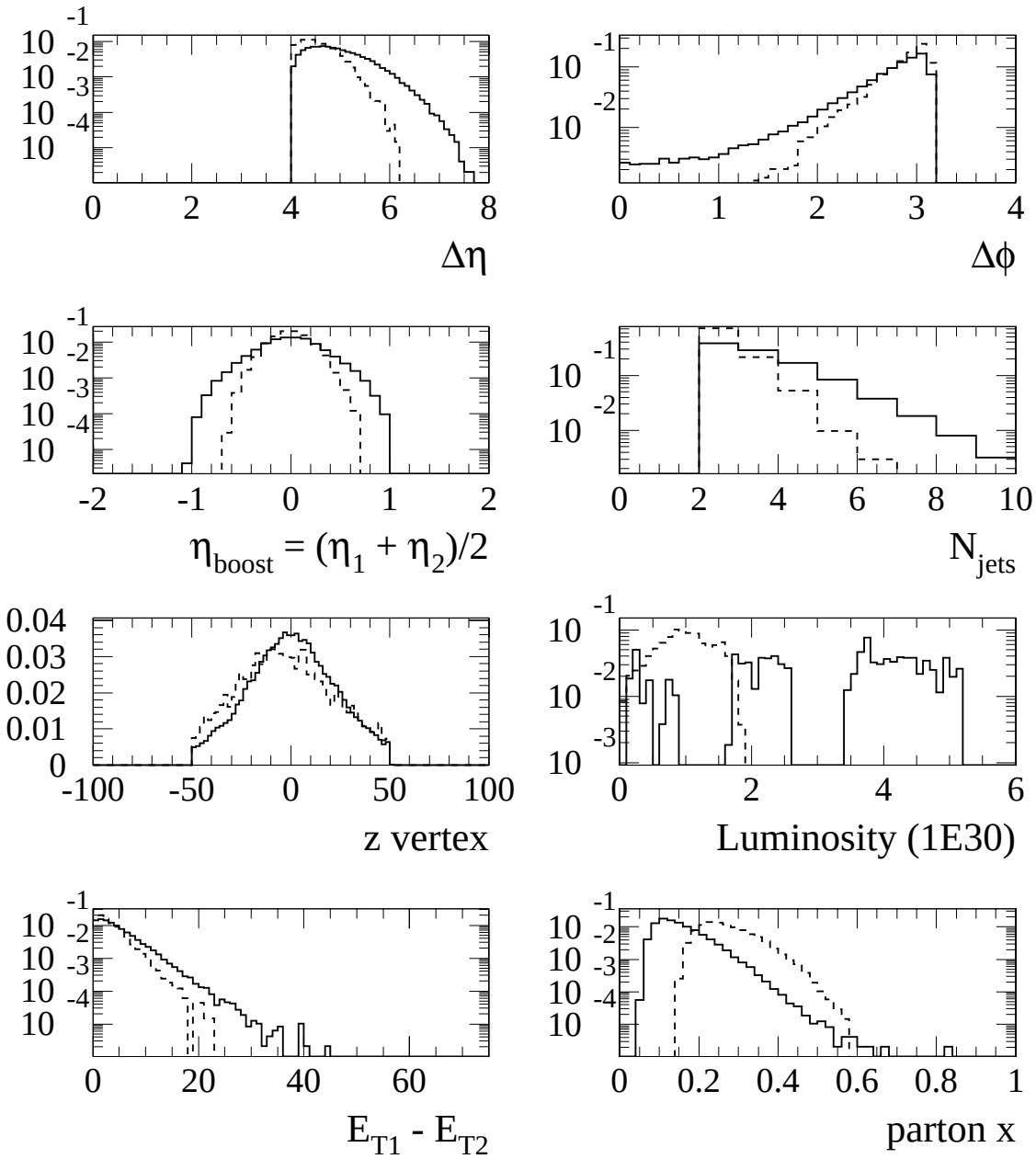

Figure 3.3. Event characteristics of the 1800 GeV and 630 GeV data samples after all cuts are applied. The solid line is 1800 GeV data; dashed is 630 GeV data.

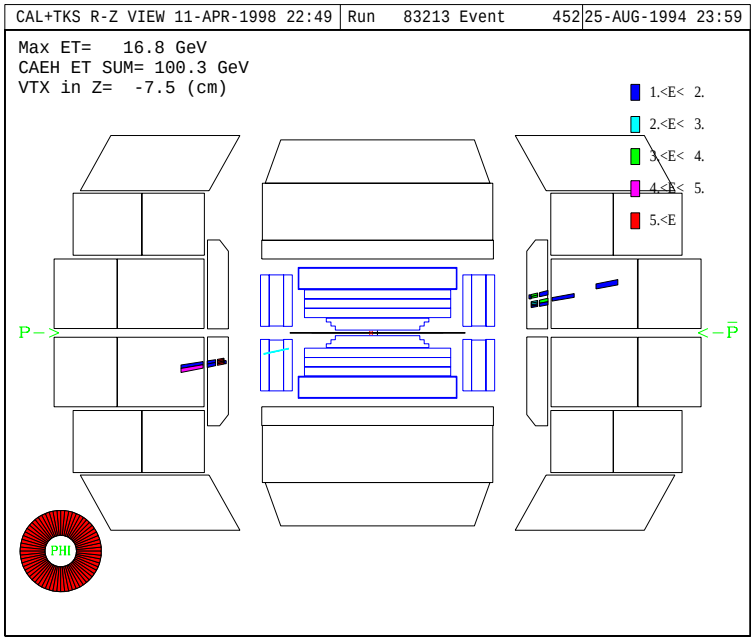

Figure 3.4. Detector event display (side view) of a rapidity gap event showing reconstructed charged particle tracks in the tracking system and energy deposition in the calorimeter.

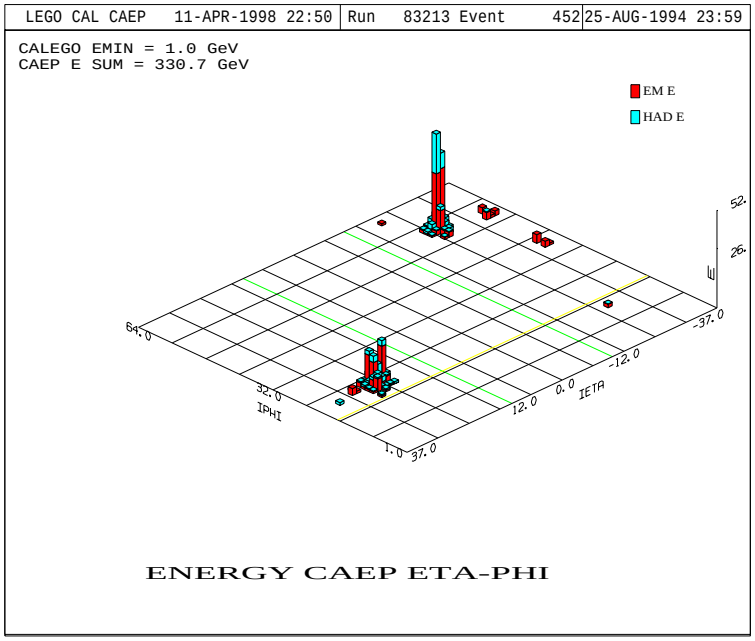

Figure 3.5. Energy deposition in the calorimeter in η vs. ϕ for a rapidity gap event. The height of each tower represents the energy deposited.

CHAPTER 4

MEASUREMENT OF THE RAPIDITY GAP FRACTION

As mentioned in the first chapter, a rapidity gap is defined as a region of rapidity in an event where particle production is highly suppressed, and color-singlet exchange is characterized by rapidity gaps between the two leading E_T jets. Therefore, counting the particle multiplicity in the rapidity region between the two leading jets is a clear method for differentiating the color-singlet exchange signal from QCD color-octet background. This method has been well-established in studies of central rapidity gaps [18, 19, 20]. The particle multiplicity is estimated experimentally by looking for energy deposits in the calorimeter or for tracks in the tracking chamber. Specifically, the multiplicities measured in this analysis are:

- n_{cal} - the number of EM calorimeter towers above a threshold of $E_T > 200$ MeV in the region $|\eta| < 1$.
- n_{trk} - the number of charged tracks in the region $|\eta| < 1$.

The multiplicity distributions can be used individually to look for rapidity gaps (n_{cal} or $n_{trk} < 2$), or the information can be combined to doubly tag rapidity gap events by requiring that both n_{cal} and n_{trk} be small.

4.1 Methods for Measuring the Fraction

Two methods have been developed for extracting the rapidity gap fraction from the event multiplicity distributions, and these are described in detail in this section.

4.1.1 Negative Binomial Fit Method

Particle multiplicity distributions have been phenomenologically parametrized well by the Negative Binomial Distribution (NBD) [31, 32]. The NBD is of the form

$$P(n;\overline{n},k) = \alpha \begin{pmatrix} n+k-1 \\ n \end{pmatrix} \left(\frac{\overline{n}}{\overline{n}+k}\right)^n \left(\frac{k}{\overline{n}+k}\right)^k \tag{4.1}$$

where $P(n)$ is the probability of observing n particles given the parameters α (a normalization factor), $\overline{n}$ (the mean multiplicity), and k, which is inversely proportional to the width of the distribution.

In the DØ Collaboration's first publication [19] of the measured rapidity gap fraction, a double NBD was fit to the calorimeter multiplicity because it parametrized the data better than a single NBD. In the original measurement, the weighting of the two NBDs was chosen by minimizing the log likelihood of the fit as a function of the normalization ratio of the two distributions. However, in the current data samples, there is no clear minimum in this log likelihood distribution. No one normalization ratio of the two distributions is significantly favored over the full range of possible combinations, and yet the resulting rapidity gap fraction that is measured from the fit shows a significant dependence on which normalization is chosen. Although, the single NBD does not parametrize the shape of the entire multiplicity distribution as well as the double NBD, fitting the leading low-multiplicity edge of the original data distribution with a single NBD results in a fractional excess in agreement with the published value. For this reason, a single NBD is used to fit to the multiplicity distributions.

Measuring Color-Singlet Signal

Fitting the n_{cal} and n_{trk} multiplicity distributions with a NBD has been shown [19] to be a good way to separate the candidate color-singlet events from the QCD background. The color-singlet signal shows up as an excess at low multiplicity on top of a smooth background that rises with multiplicity. The leading edge of a multiplicity distribution is fit with a NBD starting at a bin n_0 which gives a good χ^2/df for the fit. The fit is then extrapolated to zero multiplicity. The fraction of color-singlet events observed is represented by the rapidity gap fraction, f_s, which is defined to be the excess of events over the fit in the extrapolated region divided by the total number of events in the distribution,

$$f_s = \sum_{n=0}^{n_0-1} \frac{data(n) - fit(n)}{N_{total}}. \tag{4.2}$$

A calorimeter multiplicity distribution with a leading edge NBD fit is shown in figure 4.1, where the solid line is the fit and the dashed line is the extrapolation to zero multiplicity. The figure clearly demonstrates the excess of events above the fit in the low multiplicity region.

Leading Edge versus Full NBD

Figure 4.2 shows both a NBD fit over the entire multiplicity distribution and a NBD fit to the leading edge. The full NBD fit, shown in figure 4.2(a), does not match the multiplicity distribution very well. The full fit has a χ^2/df of 123/92, and a confidence level of less than 2%. The full NBD fit is narrower than the leading edge fit and clearly underestimates the low multiplicity background. In contrast, fitting only the leading edge of the multiplicity distribution with a NBD parametrizes the shape of the low multiplicity region well (fig 4.2(b)). The leading edge NBD fit has a

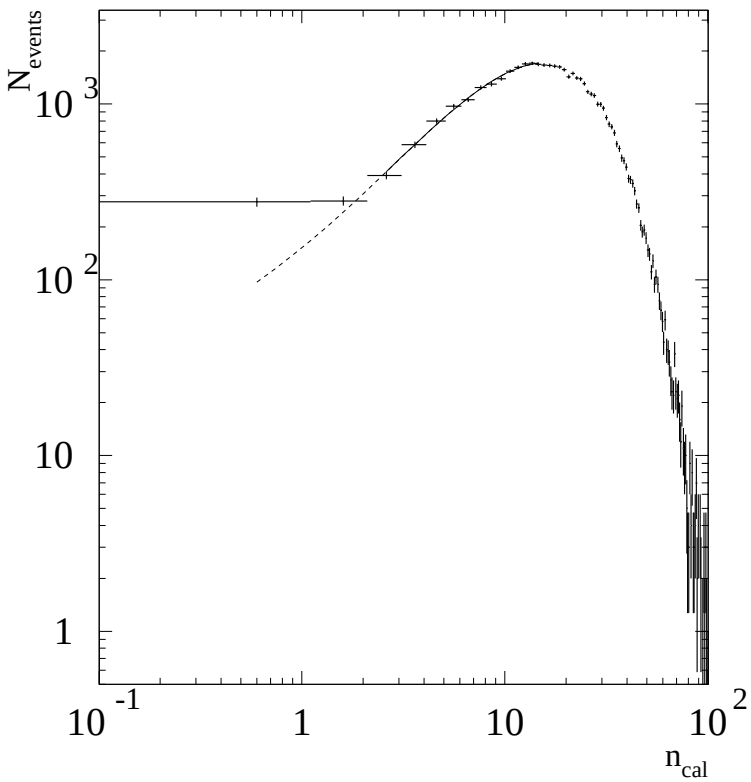

Figure 4.1. Central calorimeter multiplicity of 1800 GeV data with single NBD fit. Solid line is the fit; dashed line is an extrapolation of the fit to zero multiplicity. The log-log scale emphasizes the low-multiplicity region.

χ^2/df of 10/10 and a confidence level 45%. Figure 4.3 emphasizes the low multiplicity region of both fits. The leading edge fit is clearly superior at low multiplicities.

Using a leading edge fit also reduces the effect that multiple interaction contamination can have on extracting the fraction. Multiple interactions add to the population of higher multiplicities, shifting the mean of the distribution and adding a high multiplicity tail. Multiple interactions are more likely at higher luminosities, and figure 4.4 shows the calorimeter multiplicity for low and high luminosity data samples. Fitting only the leading edge of the multiplicity distribution agrees with the

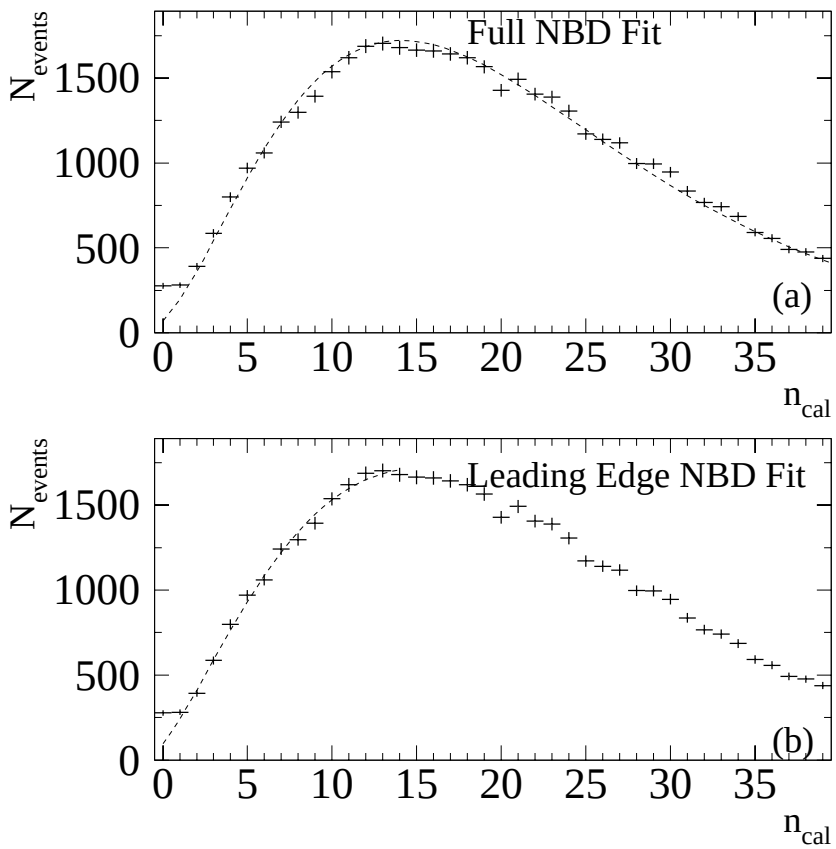

Figure 4.2. Calorimeter multiplicity with NBD fit of (a) full distribution, and (b) leading edge. Points are the 1800 GeV data.

data better in the region of interest and reduces the effects of multiple interaction contamination causing an inaccurate determination of the signal fraction.

Fitting Studies

A detailed study of the fitting method is described in reference [8] and will only be summarized here. To study the accuracy of the fitting method, an ensemble of one hundred double NBDs was generated since a double NBD can be used to parametrize the entire data sample well. The ensemble models the QCD background distribution

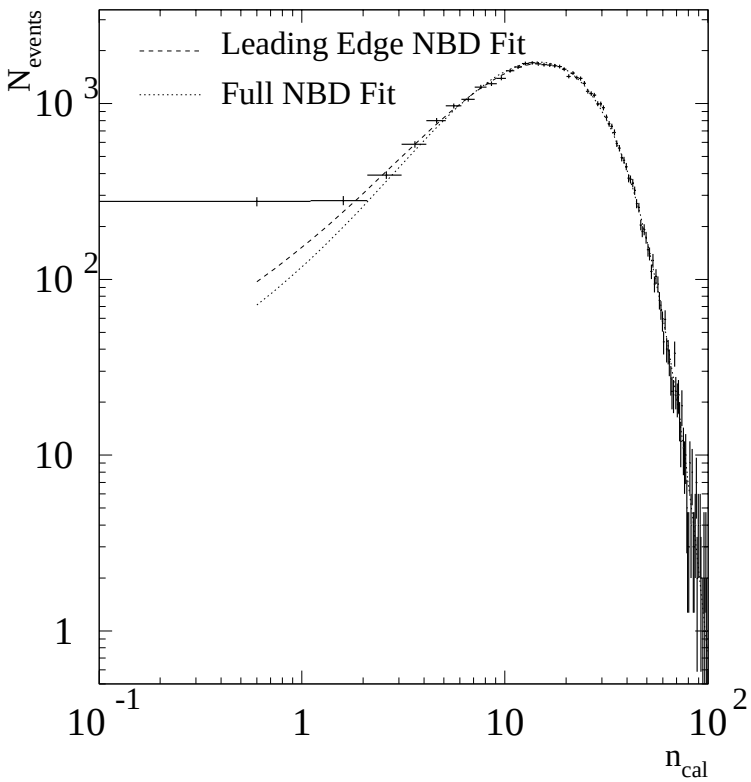

Figure 4.3. Calorimeter multiplicity for 1800 GeV data with full and leading edge NBD fit. The log-log scale emphasizes the low multiplicity region.

and by construction contains no excess at low multiplicity. The effectiveness of a single NBD to accurately fit the background distribution can be studied by applying the fitting technique to the double NBD ensemble. Each of the distributions was fit with a leading-edge single NBD for fit starting bins of $n_0 = 0$ to $n_0 = 5$. The fit ending bin was fixed at the peak of the distribution. The measured fit fraction is consistent with zero and has a good confidence limit up to $n_0 = 4$ (tables 4.1 and 4.2). The study indicates that the color-singlet fraction measurement is not dependent on the starting bin of the fit at low multiplicities; however, the starting bin will have to be chosen just beyond the region of excess in order to fit the background accurately.

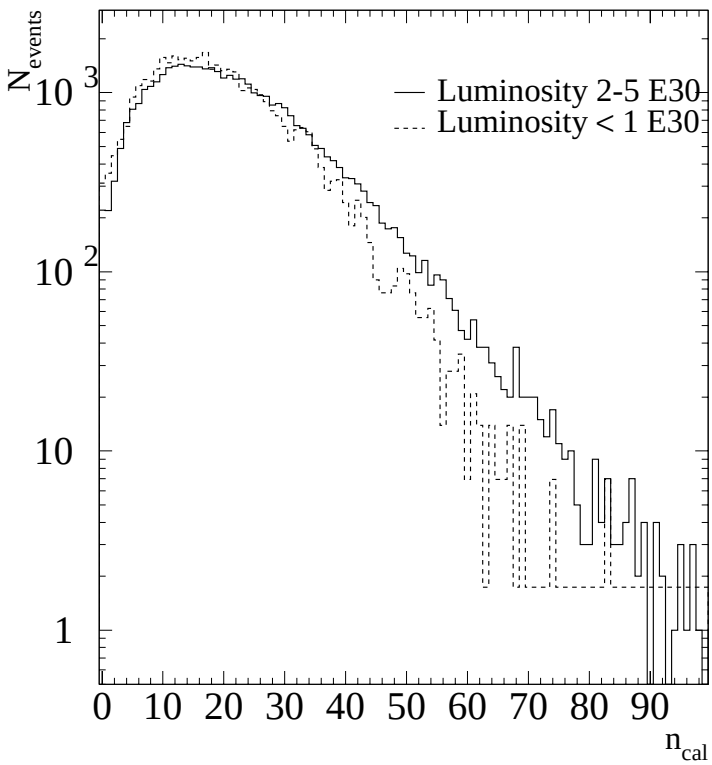

Figure 4.4. Calorimeter multiplicity distributions for 1800 GeV data at different luminosities.

The double NBD ensemble is then fit with a leading-edge single NBD from $n_0 = 2$ to ending bins in the range $n_f = 7$ to $n_f = 100$. The fit fraction, shown in tables 4.3 and 4.4, increases with increasing n_f. If the entire distribution is fit ($n_f = 100$), the fit fraction is biased giving an artificial excess of 0.15% for the 1800 GeV ensemble and 0.36% for the 630 GeV ensemble.

In conclusion, the fitting studies show that the fit starting bin should be kept as low as possible while including all of the signal, and the ending bin should be close to the peak of the distribution being fit. The studies are not used to determine an absolute fit range but are instead intended as verification that the fitting method is

TABLE 4.1

GAP FRACTION VS. FIT STARTING BIN: 1800 GeV

n_0	average $f_s(\%)$	rms	average CL(%)
0	–	–	53.48
1	0.009	0.05	54.44
2	0.012	0.12	53.28
3	0.009	0.25	52.40
4	0.058	0.51	51.92
5	0.069	0.79	49.48

TABLE 4.2

GAP FRACTION VS. FIT STARTING BIN: 630 GeV

n_0	average $f_s(\%)$	rms	average CL(%)
0	–	–	52.36
1	0.021	0.11	51.52
2	0.034	0.32	53.00
3	0.064	0.61	50.76
4	0.416	0.93	49.96
5	1.032	1.24	51.92

accurate and as a guide in selecting the starting and ending bins. Both the 630 GeV and 1800 GeV data samples are fit using starting bins of $n_0 = 2$. For the 630 GeV multiplicity distribution, the ending bin is chosen as $n_f = 11$. At 1800 GeV, the ending bin is chosen as $n_f = 14$.

4.1.2 Two-Dimensional Method

The two-dimensional plot of n_{cal} versus n_{trk} (figure 4.5) shows a clear excess in the number of events with zero tracking and zero calorimeter multiplicity. This

TABLE 4.3

GAP FRACTION VS. FIT ENDING BIN: 1800 GeV

n_f	average $f_s(\%)$	rms	average CL(%)
7	0.039	0.16	47.12
10	0.021	0.13	51.60
12	0.012	0.12	53.28
15	0.030	0.11	51.36
20	0.060	0.10	52.08
100	0.159	0.08	39.00

TABLE 4.4

GAP FRACTION VS. FIT ENDING BIN: 630 GeV

n_f	average $f_s(\%)$	rms	average CL(%)
7	0.032	0.49	47.44
10	0.013	0.37	52.84
12	0.034	0.32	53.00
15	0.086	0.27	49.60
20	0.141	0.24	46.92
100	0.356	0.19	36.16

striking excess motivated another method for measuring the rapidity gap fraction. Simply counting the fraction of events in the zero track, zero tower (0,0) bin does not require fitting, and therefore can be accurately measured for small statistical samples. When the rapidity gap fraction is measured as functions of other variables, such as jet E_T, jet $\Delta\eta$ separation, or the parton-x values, the limited statistics lead to large systematic errors in fitting the background. This new "two-dimensional" method for extracting the rapidity gap fraction improves our ability to look for dependencies on other event variables.

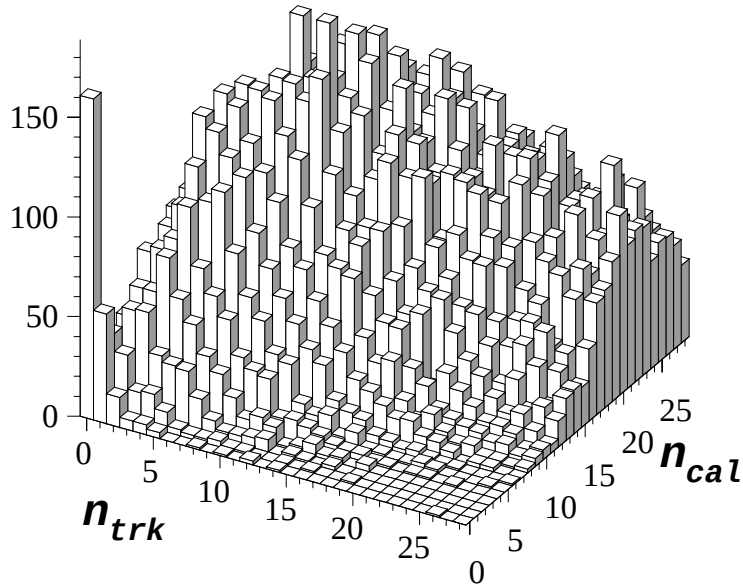

Figure 4.5. Calorimeter vs. tracking multiplicity for jet $E_T > 12$ GeV for 1800 GeV data.

The amount of background in the (0,0) bin is very small ($\sim$ 17%), but the amount of signal in that bin is only approximately 50% of the total signal. The rapidity gap fraction is thus approximated as the fraction of events in the (0,0) + (0,1) + (1,0) bins. As compared to the fit method, approximately 80% of the signal is extracted with this method. The background distribution has a slight dependence on the jet E_T and $\Delta\eta$ separation and is discussed in the following section. After background subtraction, the "two-dimensional" method can be used to study the relative shape of the rapidity gap fraction as a function of jet E_T and jet $\Delta\eta$ separation. The fraction of events in the three multiplicity bins used in the "two-dimensional" counting method is denoted

$$f^{2-D} = (N_{00} + N_{01} + N_{10})/N_{all} \tag{4.3}$$

$$f^{2-D} = f_s^{2-D} + b^{2-D} \tag{4.4}$$

where f_s^{2-D} is fraction of signal events and b^{2-D} is the fraction of background events.

4.1.3 Background Estimation and Uncertainty

In order to determine the amount of background populating the region of the multiplicity distribution where the signal fraction is measured, a data sample that contains events whose multiplicity distributions mimic those of the color-exchange background is used. The data sample requires two jets on the same side of the detector ("same-side" data). The two leading jets in this sample are required to have an $E_T > 12$ Gev, $|\eta| > 1.9$, and $\eta_1 \cdot \eta_2 > 0$. Since a LØ coincidence is required, single diffractive events which would yield a rapidity gap are largely suppressed. The same-side topology insures that the central calorimeter is, on average, highly populated with particles since there will be a color string stretched across the event. The sample may contain color-singlet exchange events, but in these events, the gap is in the forward region since it occurs between the two jets. The resulting multiplicity distribution in the central region behaves as that of color-exchange processes. Figure 4.6 shows the same-side multiplicities at 630 GeV and 1800 GeV.

An NBD is fit to both same-side multiplicity distributions using the starting and ending bins chosen for the opposite side data samples. For 1800 GeV sample, the fit has a good χ^2/df and shows that no excess is measured. For the 630 GeV sample, the fit has a good χ^2/df but measures a negative excess. The fit overestimates the number of low-multiplicity events because the mean of the distribution is low and because the number of events in the low multiplicity bins is small. Fitting the entire leading edge of the distribution also gives a good χ^2/df and measures an excess consistent with zero.

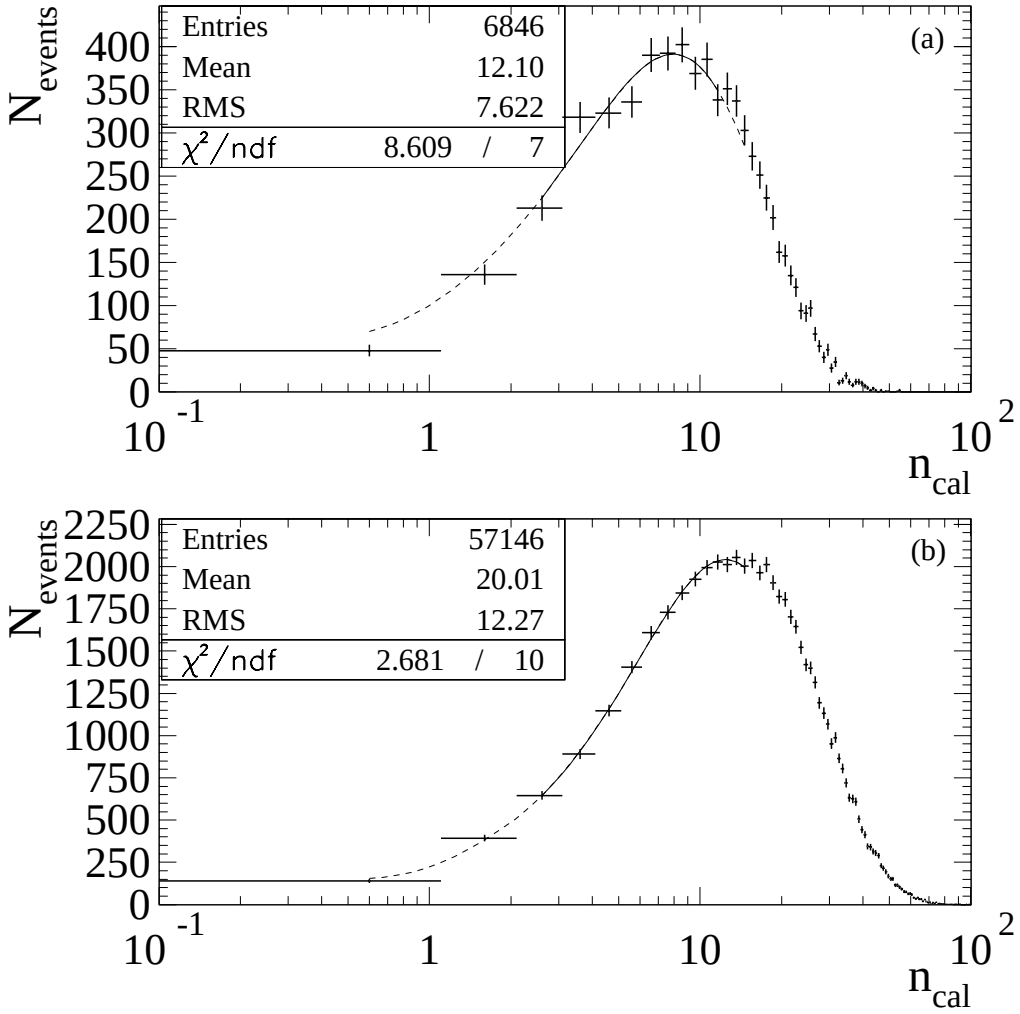

Figure 4.6. Central calorimeter multiplicity for same-side jet events at (a) 630 GeV and (b) 1800 GeV.

Figure 4.7 shows the two-dimensional n_{cal} versus n_{trk} for the same-side samples. Unlike the opposite-side distributions, there is no clear excess of low multiplicity events.

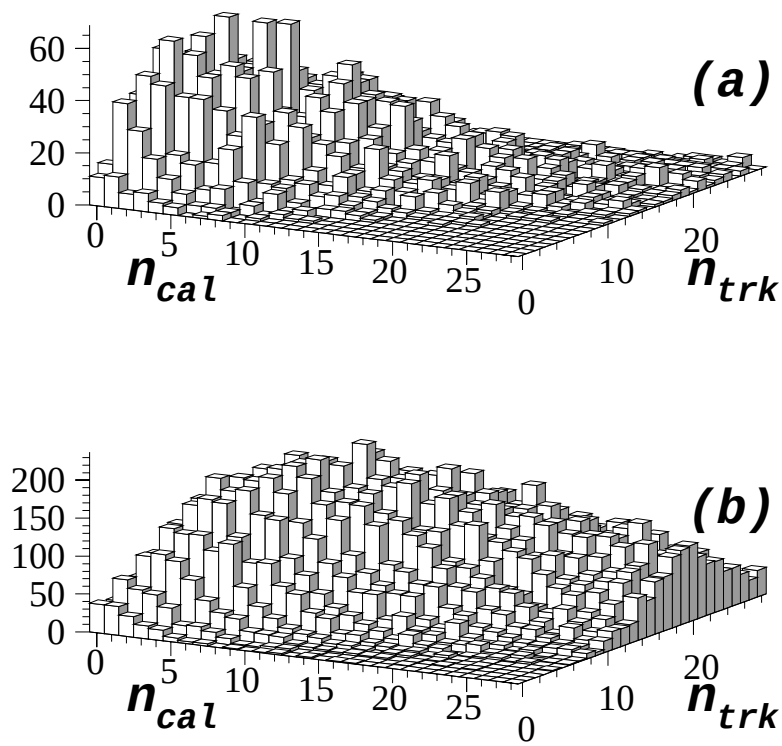

Figure 4.7. Calorimeter vs. tracking multiplicity for same-side data for (a) 630 GeV and (b) 1800 GeV.

The color-exchange background for the 2-D fraction ($b^{2-D} = b(n_{cal} + n_{trk} < 2)$) is determined using the following method.

- The NBD fit to the calorimeter multiplicity distribution is used to determine the background $b(n_{cal} < 2)$ (simply the fraction of events under the fit in the extrapolation region).

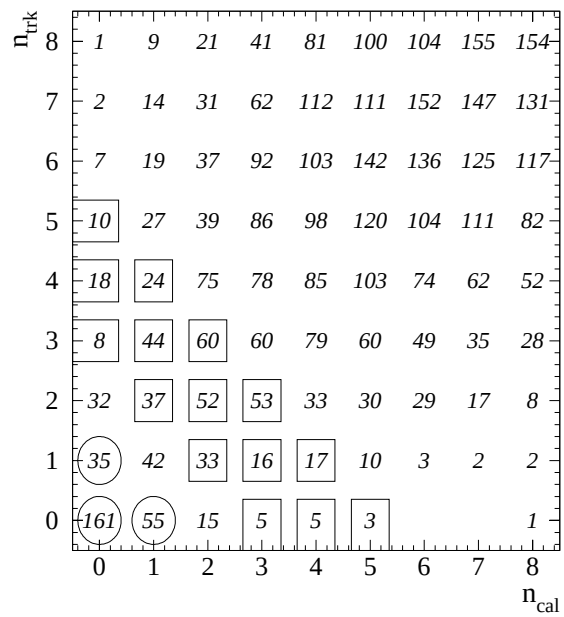

Figure 4.8. Calorimeter and tracking multiplicities for $\sqrt{s} = 1800$ GeV; Boxed entries add into background estimation; Circled entries add into signal estimation.

- $b(n_{cal} < 2)$ is corrected to a 2-D background by multiplying by the ratio of $N(n_{cal} + n_{trk} < 2)/N(n_{cal} < 2)$ obtained from the same-side sample multiplicity distribution in the same detector region (accounts for n_{cal}-n_{trk} multiplicity correlations).

- The dependence of the background on E_T and $\Delta\eta$ is determined by measuring the low-multiplicity background $b(2 < n_{cal} + n_{trk} < 6; E_T, \Delta\eta)$ from the two-dimensional opposite-side data sample. Figure 4.8 shows the number of events in each n_{cal}-n_{trk} bin included in the measurement. The color-singlet contribution in these 15 bins is negligible.

- These factors then multiply to obtain b^{2-D} as a function of E_T and $\Delta\eta$.

With this method, b^{2-D} accounts for $\sim 30\%$ of f^{2-D}.

4.2 Corrections to the Fraction

Measurement of the rapidity gap fraction is highly sensitive to multiple interaction contamination. A rapidity gap can be spoiled by even a small amount of energy (as little as one additional particle between the jets) added by a multiple interaction, and tight single interaction cuts are used in selecting the events. However, the cuts used do not remove all of the multiple interactions. This effect is corrected for and discussed in section 4.2.1. In addition, the tight single interaction cuts include a cut on the number of vertices that may actually create a bias in the rapidity gap fraction. This correction is described in section 4.2.2.

4.2.1 Luminosity

The luminosity dependence of the color-singlet fraction is discussed in detail in reference [8]. This dependence indicates that the standard event cuts used do not completely cut out multiple interactions. Therefore, a luminosity correction method was derived to correct the signal fraction to an ideal case of zero luminosity. The method used in the reference [8], however, has not been sufficient for the low E_T data, and so the method has been slightly modified.

The luminosity correction method separates the fraction into luminosity independent and dependent factors. According to this method, the color-singlet fraction is expressed as

$$f_s = \frac{\sum_{n=0}^{n_0-1} data(n) - fit(n)}{\sum_{n=0}^{n_0-1} data(n)} \left(\frac{\sum_{n=0}^{n_0-1} data(n)}{N_{total}} \right)_{Lum=0} \tag{4.5}$$

In both the $\sqrt{s}$ = 1800 and 630 GeV analyses, $n_0 = 2$. Therefore, the first factor in the correction simply takes the excess over the fit for multiplicity of 0 or 1

and divides by the total number of events in these two bins. This factor is believed to be luminosity independent since any particle added to either the first or second bin due to a multiple interaction would have the same affect on both the numerator and the denominator. Any extra minimum bias event with multiplicity greater than one would not appear in this factor. The first factor in the correction for the 1800 GeV data is 0.40 ± 0.03. For the 630 GeV data, this factor is 0.41 ± 0.04. The second factor contains the full luminosity dependence. The second factor in the correction is shown in figure 4.9 for both the 630 GeV and the 1800 GeV data.

The luminosity correction increases the rapidity gap fraction by 28% at 1800 GeV and by 15% at 630 GeV.

4.2.2 Event Vertex

The single interaction cut requires a single event vertex. Rapidity gap events have very few central tracks, and the event vertex will be reconstructed either using tracks in the Forward Drift Chambers or using timing information from the Level Ø detector. In both cases, only one vertex will be found. Making the requirement that there be only one vertex in the event does not reduce the number of signal events.

Conversely, the background events may have many central tracks. Therefore, it is possible that a single interaction could be reconstructed with more than one vertex. The single event vertex cut, therefore, may cut out perfectly good background events, arbitrarily raising the measured rapidity gap fraction.

To correct for this effect, the fraction of single vertices is found as a function of luminosity. Then, similar to the luminosity correction, the distribution is fit with a second order polynomial and extrapolated to zero luminosity. Figure 4.10 shows the fraction of single vertices for (a) signal and (b) background events at 630 GeV.

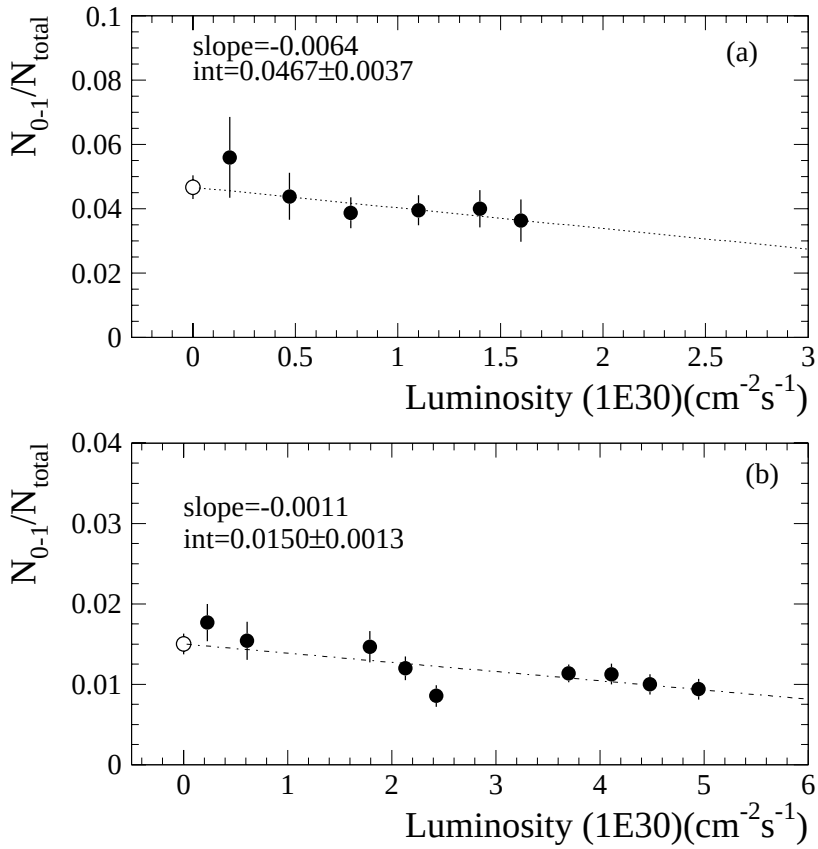

Figure 4.9. $\frac{\sum_{n=0}^{n=1} data(n)}{N_{total}}$ vs. Luminosity for (a) 630 GeV and (b) 1800 GeV.

Figure 4.11 shows the fraction of single vertices, F_v, for (a) signal and (b) background events at 1800 GeV. As expected, the fraction of single vertices for the signal events is almost identically one, whereas the fraction of single vertices for the background decreases with increasing luminosity.

The correction factor, C_{vtx} is found by dividing the intercept found for the fraction of single vertices at zero luminosity for all events by the intercept for the signal events. For the 1800 GeV data, $C_{vtx} = 0.91 \pm 0.01$ indicating that approximately 9%

of all single interactions are misidentified during the reconstruction process as having more than one vertex. For the 630 GeV data, $C_{vtx} = 0.97 \pm 0.04$ indicating that only about 3% of all single interactions are misidentified. Since the average multiplicity at 630 GeV is much lower than for 1800 GeV, the smaller number of fake extra vertices is not surprising. The correction factor has also been verified to be independent of the E_T and $\Delta\eta$ of the leading jets. Including the vertex correction factor into the luminosity corrected fraction, the color-singlet fraction becomes:

$$f_s = C_{vtx} \frac{\sum_{n=0}^{n=n_0-1} data(n) - fit(n)}{\sum_{n=0}^{n=4} data(n)} \left(\frac{\sum_{n=0}^{n=4} data(n)}{N_{total}} \right)_{Lum=0} \tag{4.6}$$

4.3 Systematics and Errors

Table 4.5 lists the systematic errors for each data sample. Contributions from each error source were calculated as follows:

TABLE 4.5

SYSTEMATIC ERRORS ON DATA

Source	630 GeV Error (%)	1800 GeV Error (%)
Jet quality cuts	3.8	3.7
MI Flag = 1 or 2	1.0	--
Out-of-cone	--	1.9
Energy Scale	3.3	3.7
Luminosity correction	8.1	16.7
N_{vertex} correction	2.2	3.7
Fit method	17.1	23.8
Total	20.0	29.6

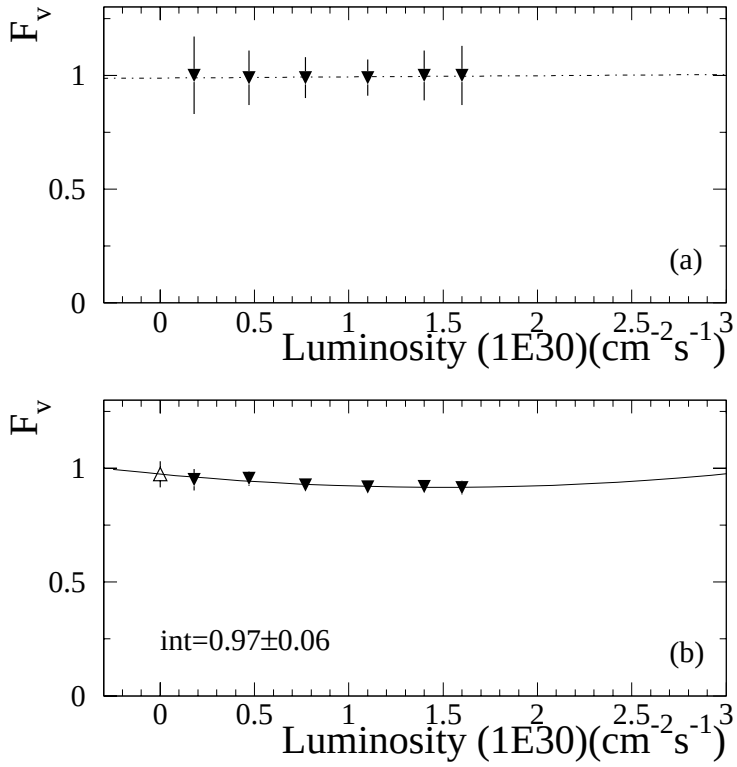

Figure 4.10. Fraction of single vertices versus luminosity for the 630 GeV data sample for (a) events with $0 \leq n_{cal} \leq 2$ (b) all events (filled triangles are high E_T data, open triangle is extrapolation of fit to zero luminosity).

- The data samples are selected by requiring that each event pass the jet quality cuts discussed in chapter 3. To study the systematic effect of this requirement, the cut was relaxed to no requirement on the jet quality, and then tightened to require that all the jets in an event pass jet quality. In each case the resulting multiplicity distribution was fit and the rapidity gap fraction was measured. The error is chosen as the largest deviation from the gap fraction with the nominal cut.

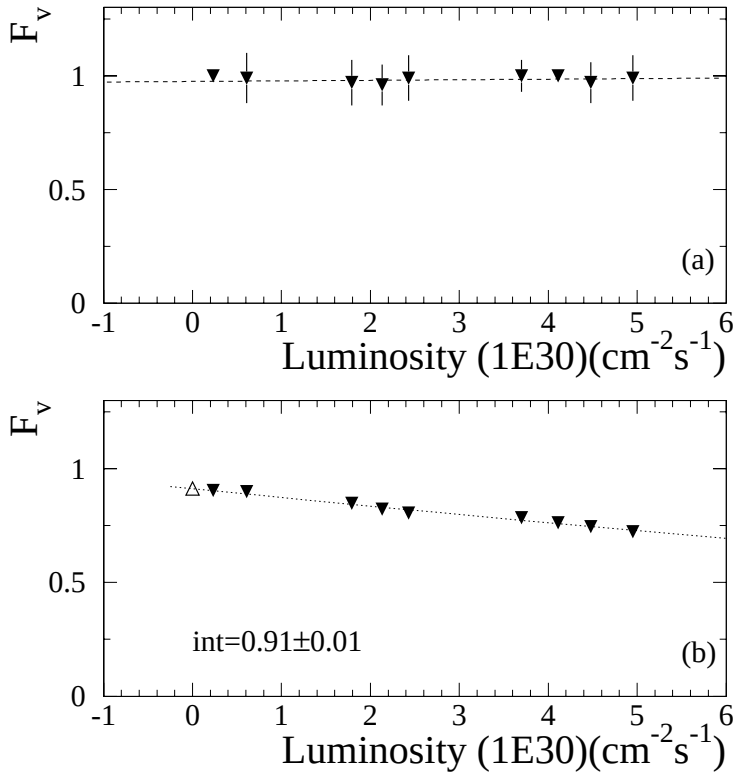

Figure 4.11. Fraction of single vertices versus luminosity for the 1800 GeV data sample for (a) events with $0 \leq n_{cal} \leq 2$ (b) all events (filled triangles are high E_T data, open triangle is extrapolation of fit to zero luminosity).

- For the 1800 GeV data, the multiple interaction flag was required online to be either zero or one. This requirement was made offline on the 630 GeV data. To study the effect of this offline requirement, the multiple interaction flag cut was loosened to include flag values of two. The resulting multiplicity distribution was fit and the gap fraction was measured. The error is the deviation from the gap fraction with the standard cuts.

- Out-of-cone effects were studied by converting the jet physics η to detector η. Although central rapidity gap events tend to have small η-boost, a boosted event could spoil a gap if the jet positions are measured in physics η. Our studies revealed negligible out-of-cone effects.

- The analysis uses the CAFIX 5.0 energy scale. Selecting jets using the low, nominal, or high energy scale correction has little effect on the measured gap fraction. The error assigned is the maximum deviation from the gap fraction using the nominal energy scale correction. The gap fractions have also been measured using CAFIX 5.1 (the most recent energy scale correction) [24, 25] and the results are in agreement with those found using CAFIX 5.0.

- The errors on the luminosity correction and vertex correction mentioned in the previous section are added into the total systematic error. The error on each correction is simply the error on extrapolating the fit to an intercept at zero luminosity.

- The largest systematic error is due to the fitting method used for extracting the signal fraction. Studies of the fitting method were discussed previously. The error on the fitting is determined by adding two contributions in quadrature. The first component is the rms of the distribution of fit fractions found from fitting the generated double NBD ensembles. The second component is the deviation in the fit fraction when the data is fit using a starting bin that has been increased by one.

CHAPTER 5

RESULTS AND INTERPRETATIONS

In this chapter, results are presented on the measurement of the color-singlet fraction as a function of jet E_T, jet $\Delta\eta$ separation, parton x, and center-of-mass energy (630 and 1800 GeV). Results using both the NBD fitting method and the two-dimensional method for extracting the rapidity gap fraction are discussed.

5.1 Measurement of the Color-Singlet Fraction

The rapidity gap fraction, f_s, is measured using the central calorimeter multiplicity ($|\eta| < 1$). A single NBD is fit to the leading edge of the calorimeter tower multiplicity distribution, and the excess over the fit in the first two bins divided by the total number of events is the measured color-singlet fraction. The measured color-singlet fractions at 630 GeV and 1800 GeV are

$$f_s{}^{630} = (1.85 \pm 0.09(stat) \pm 0.18(syst.cuts) \pm 0.32(syst.fit))\%$$

$$= (1.85 \pm 0.38)\%$$

$$f_s{}^{1800} = (0.54 \pm 0.06(stat) \pm 0.10(syst.cuts) \pm 0.13(syst.fit))\%$$

$$= (0.54 \pm 0.17)\%.$$

The ratio (R^{630}_{1800}) of these two fractions is 3.43 ± 1.29, a 1.9σ deviation from one. The difference (D^{630}_{1800}) of these two fractions is 1.31 ± 0.42, a 3.1σ deviation from zero. Both fractions include the luminosity correction and the vertex correction discussed in chapter 4.

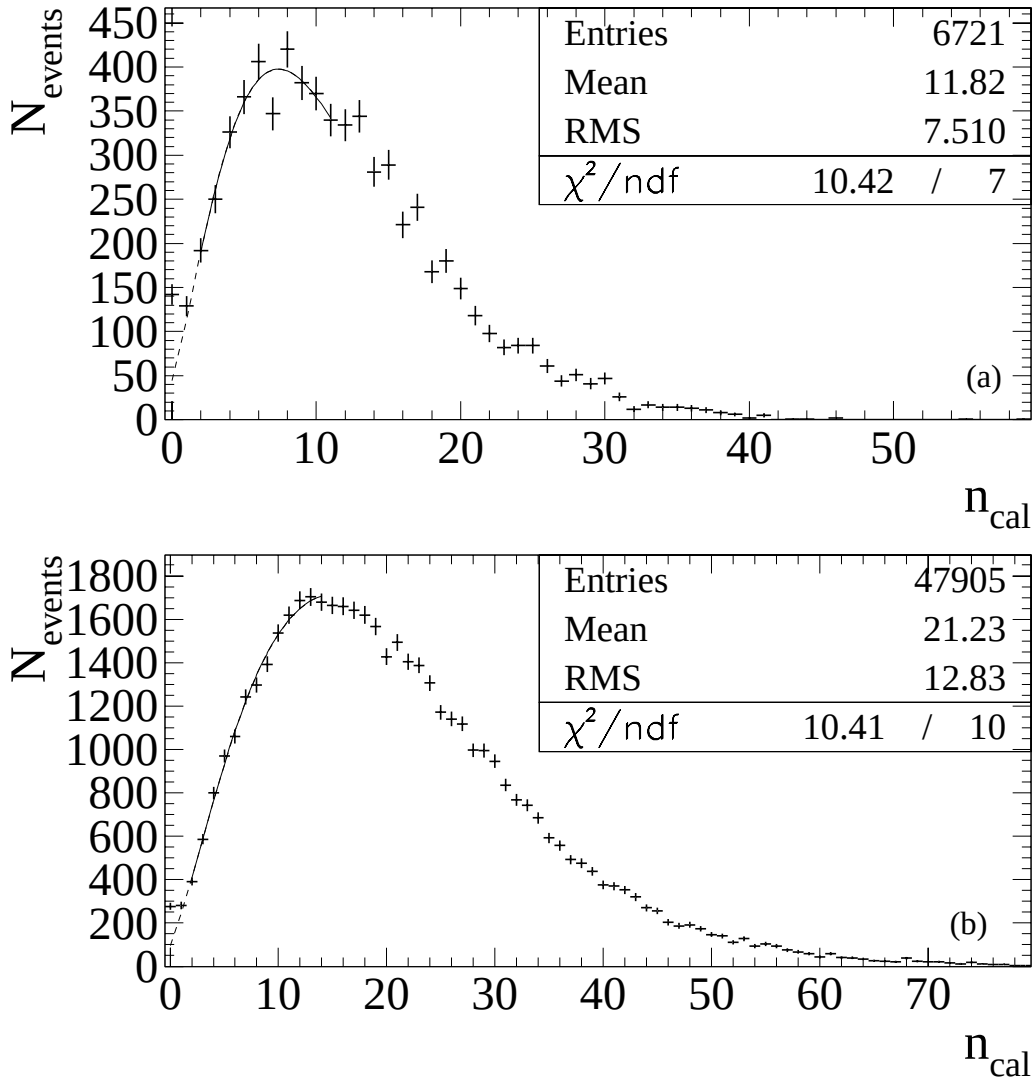

Figure 5.1. Central calorimeter multiplicity with single NBD fit for (a) 630 GeV data and (b) 1800 GeV data. Note the excess over the extrapolated fit in the first two bins.

Figure 5.1 shows the fitted multiplicity distributions for each center-of-mass energy. Particle production occurs at a lower rate at the lower center-of-mass energy. This effect is demonstrated by the lower mean multiplicity.

Many cross checks were performed to test the robustness of the measured color-singlet fraction. These are described in the following sections.

5.1.1 Dependence on Tower Threshold

In order to study the effect a lower mean multiplicity might have on fitting the distribution and extracting the fraction, the calorimeter tower threshold was varied for the 1800 GeV data sample. The thresholds were varied from 200 MeV to 350 MeV. The resulting multiplicity distributions, shown in figure 5.2, are each fit with a NBD and the rapidity gap fraction is measured. Figure 5.3 shows the measured color-singlet fraction using the NBD fit as a function of calorimeter tower threshold. In the plot, the gap fractions have been corrected for vertex and luminosity (see section 3.2) and only statistical errors are included. The color-singlet fraction is shown to be independent of the tower threshold, although there is some fluctuation with increasing threshold values. As seen in figure 5.2, the mean of the multiplicity distribution decreases as the tower threshold increases. This reduces the reliability of extracting an accurate gap fraction using the NBD fitting method; the amount of background under the signal increases and the leading edge of the distribution decreases, resulting in larger fitting errors. Using a higher calorimeter tower threshold produces a rapidity gap fraction that is well within errors of the standard value using a threshold of 200 MeV.

Using a tower threshold of 270 MeV for the 1800 GeV data, the resulting leading edge of the multiplicity distribution can be matched to the leading edge of the 630 GeV multiplicity distribution. Figure 5.4 shows the two distributions overlayed, and reinforces that the higher signal fraction found at 630 GeV is not a function of having a lower mean multiplicity. The ratio of these two fractions is 3.4 ± 0.7(stat).

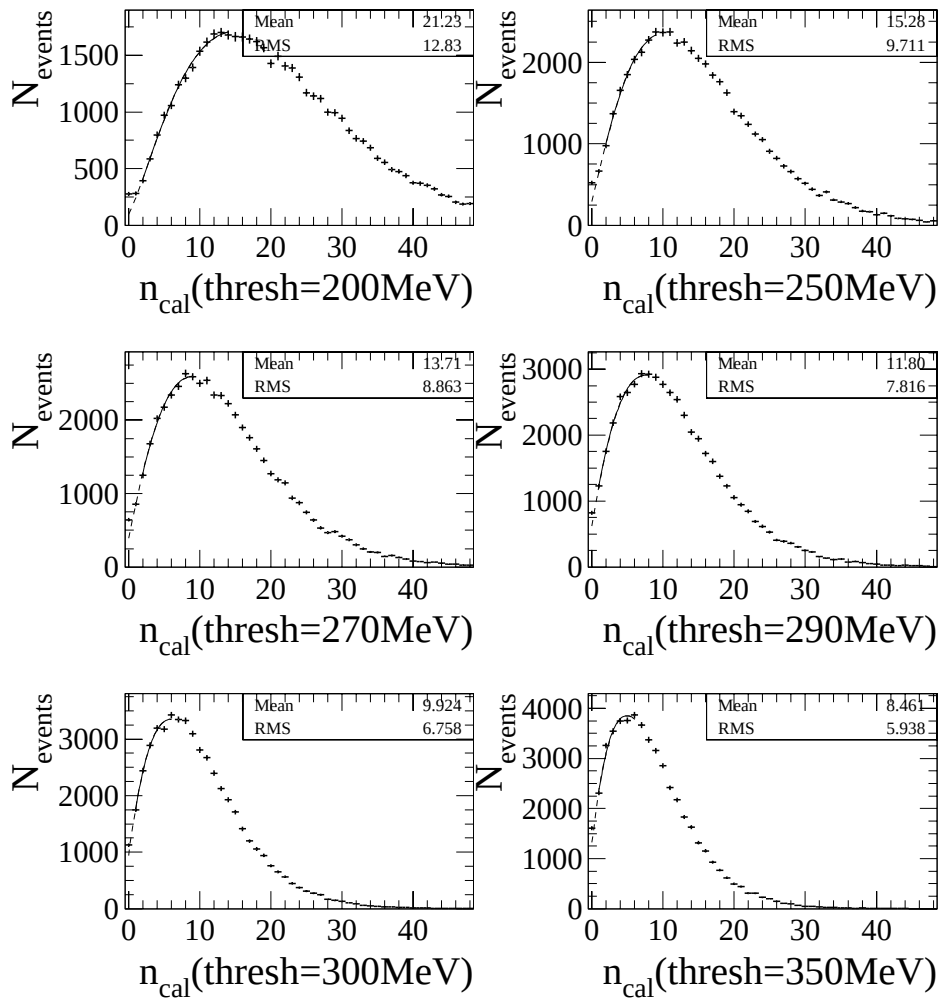

Figure 5.2. Calorimeter multiplicities for 1800 GeV data with varying tower thresholds.

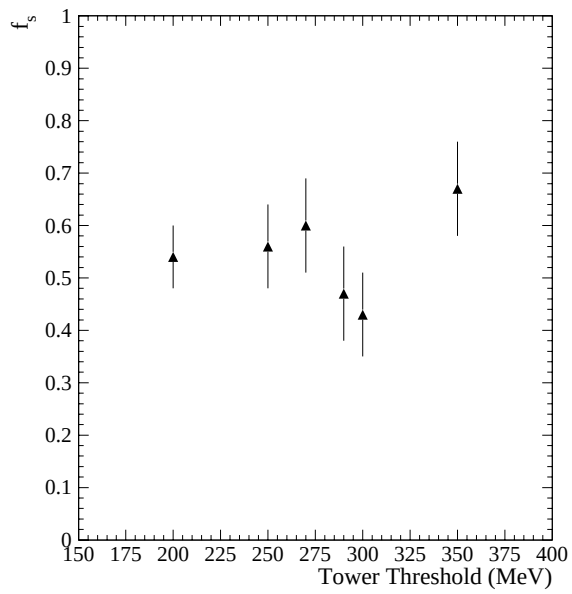

Figure 5.3. The rapidity gap fraction as a function of calorimeter tower threshold for the 1800 GeV data.

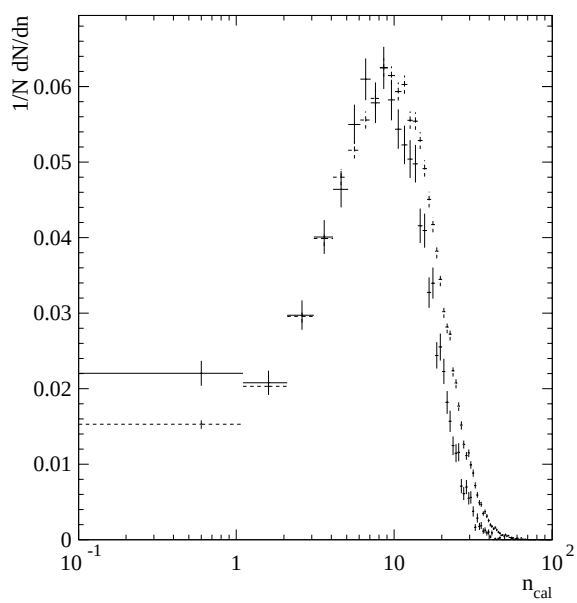

Figure 5.4. An overlay of the 630 GeV calorimeter multiplicity distribution using a tower threshold of 200 MeV (solid curve) with multiplicity at 1800 GeV using a tower threshold of 270 MeV (dashed curve).

5.1.2 f_s from Central Tracking Multiplicity

As another check, the central tracking multiplicity, n_{trk}, can be fit and the color-singlet fraction extracted. The measured fractions, including the luminosity and vertex corrections, found from the central tracking are

$$f_s{}^{630} = (1.84 \pm 0.38)\%$$

$$f_s{}^{1800} = (0.52 \pm 0.16)\%$$

and are in excellent agreement with the color-singlet fractions found using the calorimeter multiplicities. Figure 5.5 displays the fitted tracking multiplicity in the central region for both center-of-mass energy data sets.

5.1.3 f_s for 2-Jet Events

Typically, color-singlet events tend to be 2-jet events due to the imposed restriction on color flow between the two leading jets. However, the color-octet background events can have a higher average number of jets. By allowing events to have any number of jets above two, the denominator (background) events include higher orders of radiation whereas the numerator (signal) events are mainly $2 \rightarrow 2$ processes. It is of interest, therefore, to restrict the background events to also be $2 \rightarrow 2$ processes and measure the color-singlet fraction. By restricting higher orders of radiation, it is expected that the color-singlet fraction be somewhat larger than that found without such a restriction. Indeed, the measured color-singlet fractions for strictly 2-jet events are

$$f_s{}^{630} = (2.55 \pm 0.52)\%$$

$$f_s{}^{1800} = (1.42 \pm 0.36)\%.$$

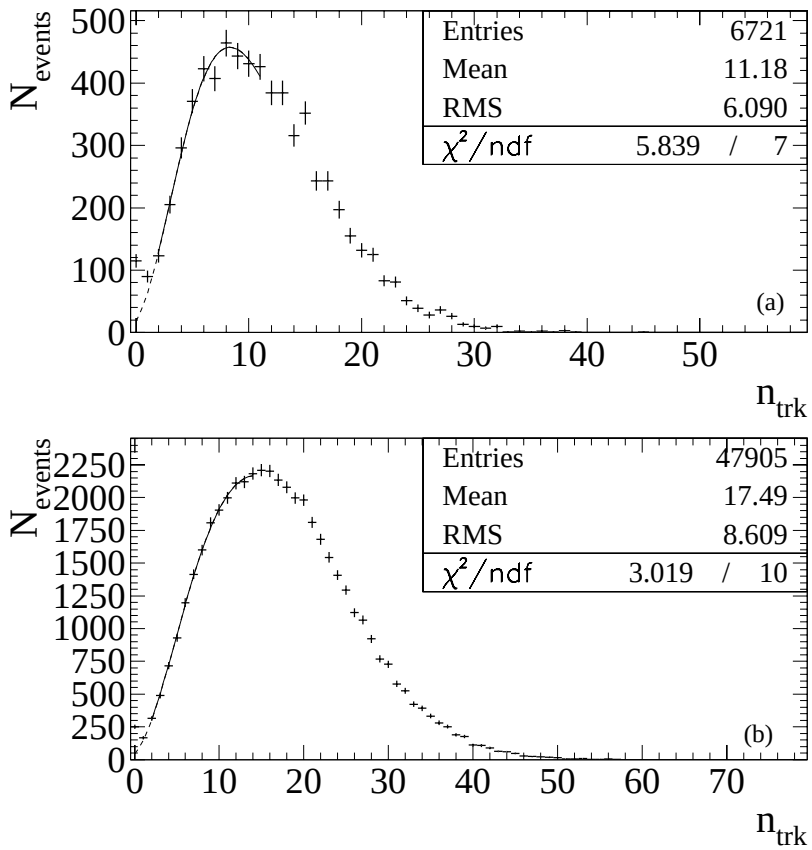

Figure 5.5. Fit of central tracking multiplicity for (a) 630 GeV and (b) 1800 GeV data.

The ratio of these two fractions is 1.8 ± 0.6, a 1.3σ deviation from one. The difference of these fractions is 1.1 ± 0.6, a 1.8σ deviation from zero. The central tracking multiplicity distributions of the 2-jet events were also fit at each center-of-mass energy, and the measured fractions agree within errors with the above results.

5.1.4 Color-Singlet Fraction from Two Dimensional Method

As mentioned in the previous chapter, the two-dimensional method after background subtraction accepts approximately 80% of the color-singlet fraction compared

to the fitting method. Therefore, this method is not preferred over the fitting method for the determination of the actual value of the color-singlet fraction. Rather, the two-dimensional method is preferred for obtaining the shape of the fraction's dependence on jet E_T, jet $\Delta\eta$ separation, and parton x. However, the color-singlet fraction can be approximated as f_s^{2-D} for each center-of-mass energy, and the ratio can be found as another cross check.

The approximate color-singlet fractions using the two-dimensional method before background subtraction but including the luminosity and vertex corrections are

$$f_s^{2-D}(630) = (2.15 \pm 0.20(stat))\%$$

$$f_s^{2-D}(1800) = (0.61 \pm 0.04(stat))\%$$

The ratio (R_{1800}^{630}) of these two fractions is 3.52 $\pm$ 0.40(stat). The difference (D_{1800}^{630}) of these two fractions is 1.54 $\pm$ 0.20(stat). After background subtraction, the color-singlet fractions are

$$f_s^{2-D}(630) = (1.61 \pm 0.15(stat))\%$$

$$f_s^{2-D}(1800) = (0.46 \pm 0.03(stat))\%$$

These fractions are 85% of the gap fractions found using the NBD fit. The ratio (R_{1800}^{630}) of these two fractions is 3.5 $\pm$ 0.4(stat). The difference (D_{1800}^{630}) of these two fractions is 1.10 $\pm$ 0.15(stat).

5.1.5 Interpretation of f_s

All of the above measurements of f_s show that the fraction of color-singlet exchange is larger for the 630 GeV data than for the 1800 GeV data. This result is inconsistent with the prediction of the naive two-gluon model which states that because a two-gluon color-singlet couples more strongly to gluons than to quarks, the

ratio of the rapidity gap fraction at 630 GeV to that at 1800 GeV would be less than one. In contrast, the ratio of rapidity gap fractions of the two center-of-mass energies is consistent with the predictions of the color rearrangement model for color-singlet exchange.

5.2 Color-Singlet Fraction Versus Jet E_T

The measurement of the color-singlet fraction as a function of the E_T of the leading jets uses the $\sqrt{s}$ = 1800 GeV data presented in this thesis in combination with the data presented in reference [8]. The data for this analysis contributes the lowest E_T point in the range studied. For this measurement, the low E_T jets are required to have 15 GeV $< E_T <$ 25 GeV. This subset is roughly 50% of the full low E_T data sample. The data in reference [8] contributes one point from a medium E_T (25 GeV $< E_T <$ 30 GeV) data set, and six points from a high E_T ($E_T >$ 30 GeV) data set. The measurement of the color-singlet fraction versus jet E_T was presented in reference [8], but is also presented here since the method for extracting both f_s^{2-D} and b^{2-D} have changed slightly and final errors have been calculated for the low E_T point. Figure 5.6 shows the calorimeter multiplicity distributions for the three data samples. Looking at the low multiplicity region of the distributions shows that the high E_T sample clearly has more low multiplicity events than the low E_T sample.

Figure 5.7 shows the fraction f^{2-D} and the background b^{2-D} versus jet E_T. The data is binned as a function of the second-leading jet E_T, and the points are plotted at the average E_T of the two leading jets. Many different binning methods were studied in reference [8]. This binning was selected since it keeps the acceptance bias in E_T across the E_T bins at a minimum by keeping the ΔE_T fixed for each bin. The

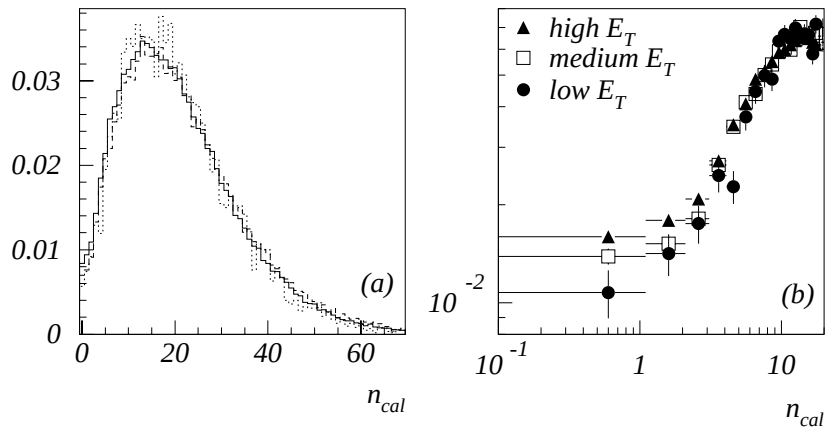

Figure 5.6. Central calorimeter multiplicities for three E_T samples: (a) Solid line is high E_T; dashed line is medium E_T; dotted line is low E_T (b) log-log scale emphasizes the low multiplicity region.

two lowest E_T f^{2-D} points include inner statistical error bars and outer systematic error bars. The high E_T f^{2-D} points include statistical error bars and an overall systematic error normalization band. All of the b^{2-D} points include both statistical and systematic errors. All of the points, f^{2-D} and b^{2-D}, have been corrected with the luminosity and vertex corrections. Figure 5.8 shows the background subtracted color-singlet fraction, f_s^{2-D} versus jet E_T. Table 5.1 shows detailed information about each bin. The parton x is calculated from jet kinematic quantities according to

$$x = \sum_{i=1}^{N_{jets}} \frac{E_{Ti}}{\sqrt{s}} e^{\eta_i}. \tag{5.1}$$

Since the two leading jets in each event are in opposite hemispheres of the detector, their x values are very similar. For this reason, instead of finding an x value for each jet and then averaging, only one x value is found for each event by summing over all the jets. This x definition has been compared with other definitions and the results are presented in a later section.

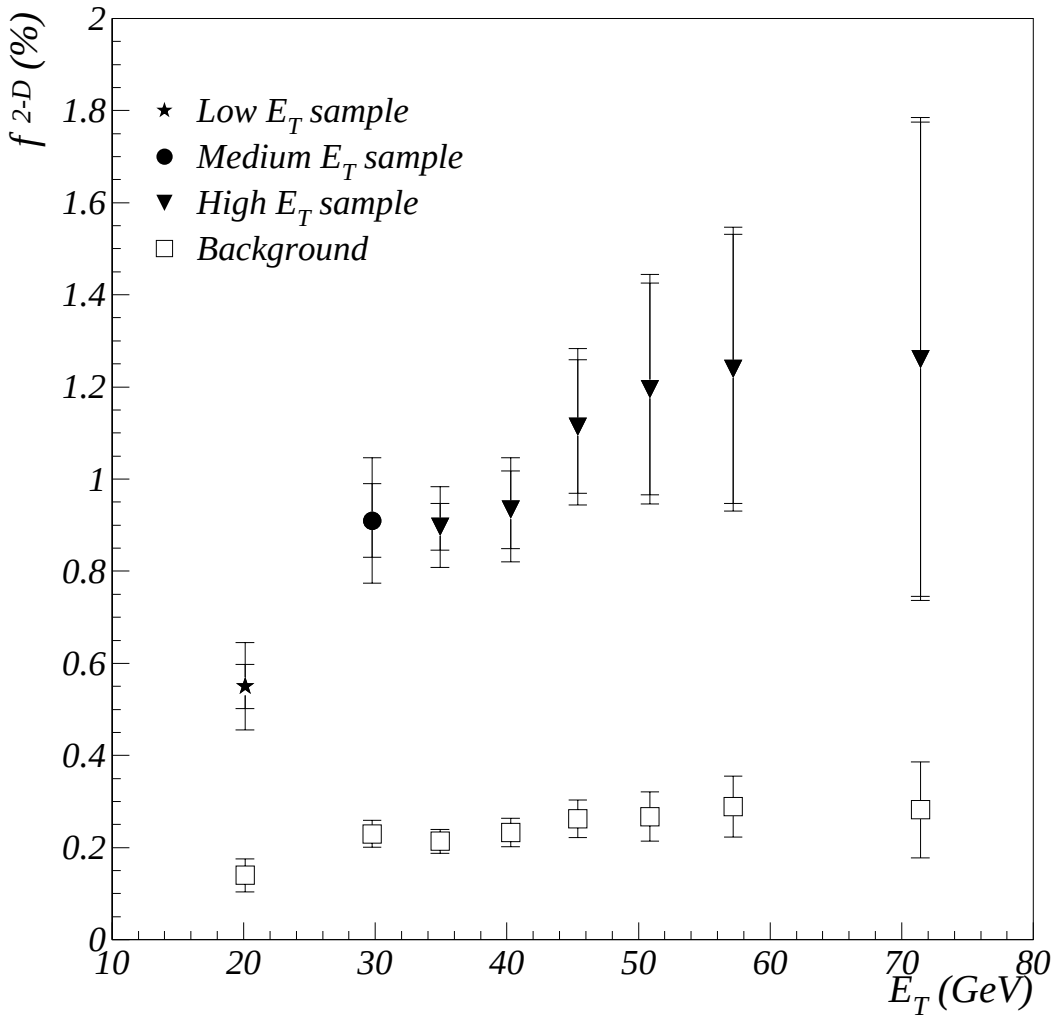

Figure 5.7. Upper data are f^{2-D} as a function of jet E_T for 1800 GeV data. The two lowest E_T points include inner statistical error bars and outer systematic error bars. High E_T points include statistical error bars and an over all systematic normalization error represented by the hatched area. Lower data are the background, b^{2-D}, and include total error bars.

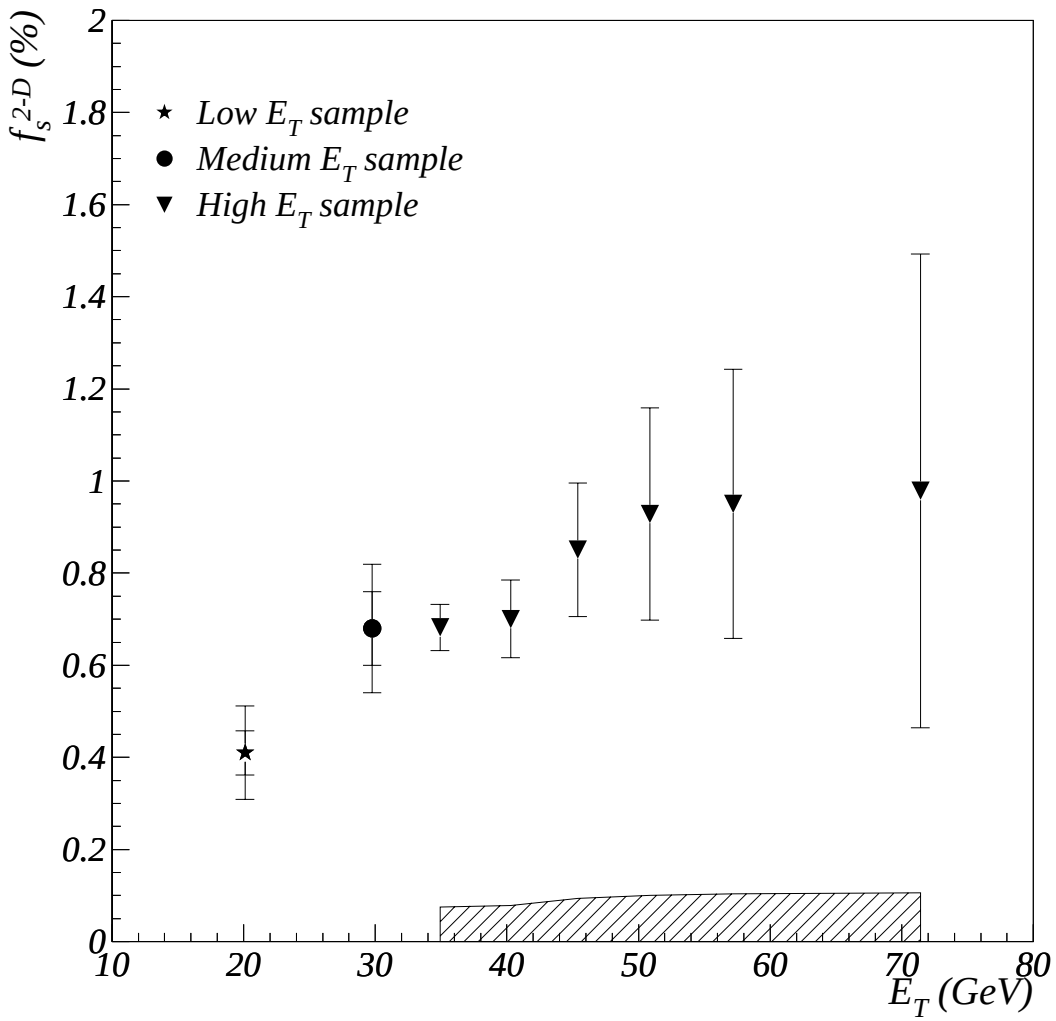

Figure 5.8. f_s^{2-D} as a function of jet E_T for 1800 GeV data. The two lowest E_T points include inner statistical error bars and outer systematic error bars. High E_T points include statistical error bars and a systematic normalization error represented by the hatched area.

TABLE 5.1

CHARACTERISTICS OF f_s^{2-D} VS. JET E_T

E_T bin (GeV)	$< E_T >$	$< \|\eta\| >$	$f_s^{2-D}(\%)$	N_{event}	x	$\%Q$
$15-25$	20.1	2.46	0.41 ± 0.10	23751	0.147	61
$25-30$	29.8	2.39	0.68 ± 0.14	21579	0.211	69
$30-35$	34.9	2.35	0.68 ± 0.09	44643	0.237	71
$35-40$	40.3	2.32	0.70 ± 0.12	16809	0.261	74
$40-45$	45.4	2.29	0.85 ± 0.17	6735	0.284	76
$45-50$	50.9	2.28	0.93 ± 0.25	2885	0.308	78
$50-60$	57.2	2.25	0.95 ± 0.31	1855	0.333	81
> 60	71.4	2.22	0.98 ± 0.52	609	0.395	85

Note: x is parton-x fraction and $\%Q$ is percent of initial quarks using the CTEQ3M pdf[2].

5.2.1 Interpretation of f_s^{2-D} vs. Jet E_T

The rapidity gap fraction is shown to increase slightly with increasing jet E_T. To understand this dependence more quantitatively, linear fits were performed on the background subtracted fraction (figure 5.8). Both a line with a slope and a line with zero slope are good fits; however, the line with zero slope has a lower confidence level. The zero slope fit is $f_s = (0.65 \pm 0.05)\%$ and has a $\chi^2/df = 11.5/8$ which corresponds to a confidence level of 18%. The linear fit with a slope is $f_s = ((0.015 \pm 0.005)E_T + (0.15 \pm 0.17))\%$ and has a $\chi^2/df = 1.3/8$ which corresponds to a confidence level of 99%. Since both the naive two-gluon model and the BFKL calculation predict that the color-singlet fraction should decrease with increasing jet E_T, these results appear to be inconsistent with these models. The data may be consistent with the soft color

rearrangement model, however, since this model predicts an increase in the rapidity gap fraction as jet E_T increases.

5.3 Color-Singlet Fraction Versus $\Delta\eta$

The gap fraction before background subtraction and the background using the two-dimensional method is shown as a function of the jet $\Delta\eta$ separation in figure 5.9. The background subtracted color-singlet fraction is shown in figure 5.10. Since only one data sample is used for this plot, the points include statistical errors only; the systematic error is 15% and includes the systematic error on the cuts applied and the error on the luminosity and vertex corrections. Therefore, the systematic error is independent of $\Delta\eta$ and is simply an overall normalization uncertainty on the distribution of points. The characteristics for each of the $\Delta\eta$ bins is given in table 5.2.

TABLE 5.2

CHARACTERISTICS OF f_s^{2-D} VS. JET $\Delta\eta$ SEPARATION

$\Delta\eta$ bin	$<\Delta\eta>$	$<E_T>$	$f_s^{2-D}(\%)$	N_{events}	x	$\%Q$
$4.0-4.3$	4.18	22.1	0.38 ± 0.16	4000	0.121	56
$4.3-4.6$	4.45	21.5	0.29 ± 0.11	6835	0.134	58
$4.6-5.0$	4.79	21.2	0.46 ± 0.12	8761	0.154	62
$5.0-5.4$	5.19	20.9	0.47 ± 0.15	5886	0.184	66
$5.4-5.8$	5.58	20.4	0.52 ± 0.23	3133	0.215	69
>5.8	6.09	19.6	0.67 ± 0.31	1737	0.261	74

Note: x is parton-x fraction and $\%Q$ is percent of initial quarks using the CTEQ3M pdf[2].

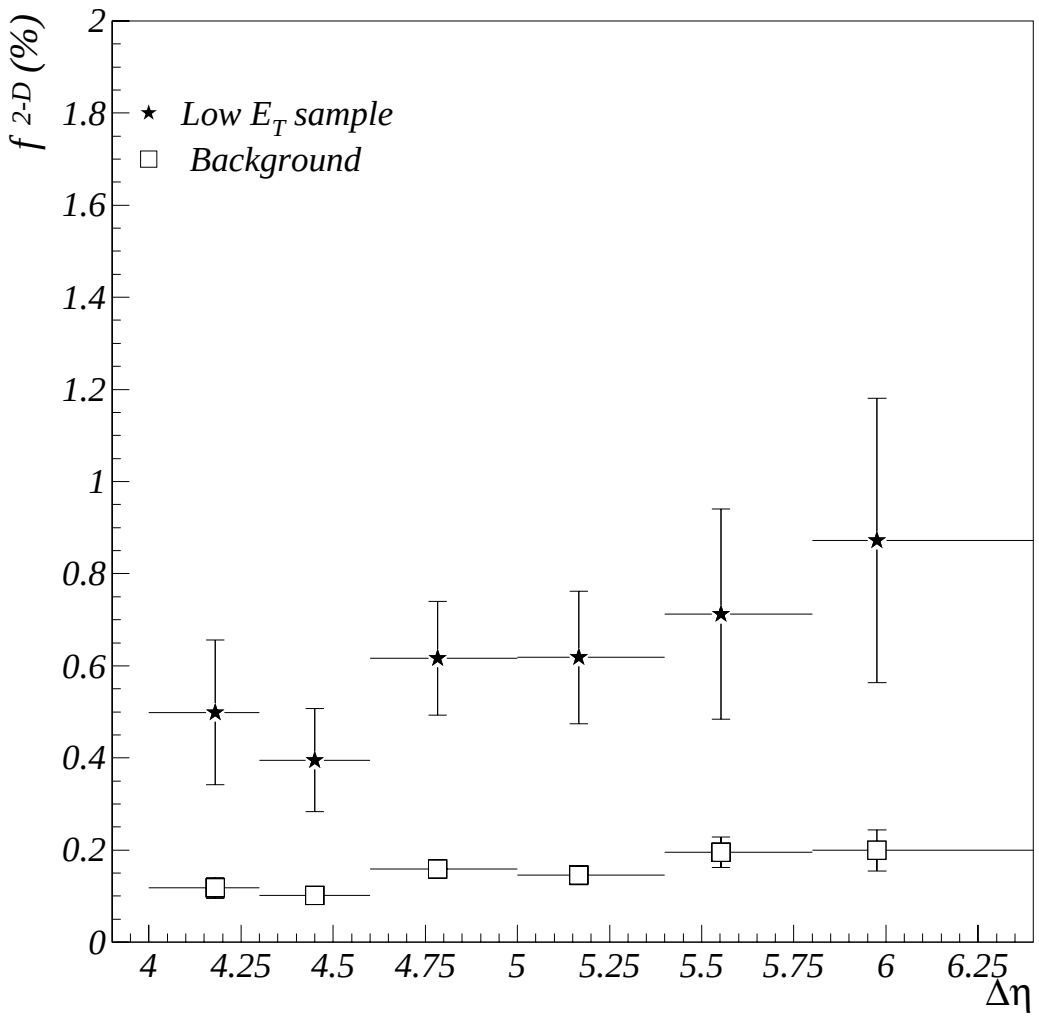

Figure 5.9. Upper data are f^{2-D} as a function of jet $\Delta\eta$ separation for 1800 GeV data. Lower data are background, b^{2-D}, for these $\Delta\eta$ bins. Errors are statistical.

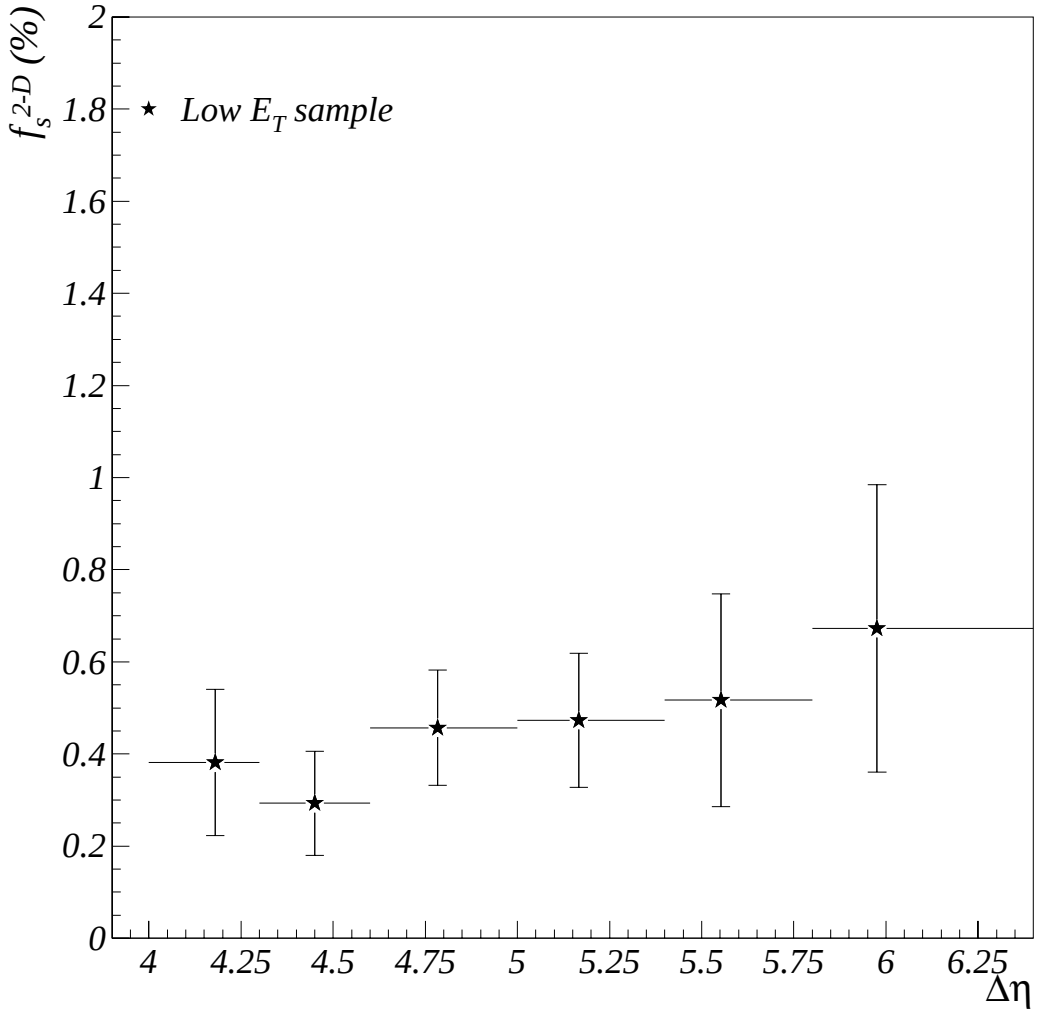

Figure 5.10. f_s^{2-D} as a function of jet $\Delta\eta$ separation for 1800 GeV data. Errors are statistical.

5.3.1 Interpretation of f_s^{2-D} vs. $\Delta\eta$

The gap fraction versus $\Delta\eta$ has a slight rise with increasing $\Delta\eta$ values. Again, this data was fit with straight line curves. When fit with a line of zero slope, the resulting fit is $f_s = (0.41 \pm 0.07)\%$ and has a $\chi^2/df = 2.22/6$ which corresponds to a confidence level of 89%. When a line with slope is used, the resulting fit is $f_s = ((0.17 \pm 0.15)\Delta\eta + (-0.40 \pm 0.71))\%$ and has a $\chi^2/df = 0.83/6$ which corresponds to a confidence level of 98%. Both fits are good.

The BFKL calculation predicts an increase in the color-singlet fraction with increasing $\Delta\eta$ at very high, but unspecified, $\Delta\eta$. The soft color rearrangement model also predicts an increasing color-singlet fraction with increasing $\Delta\eta$. The data are possibly consistent with both of these models. The data are inconsistent with the naive two-gluon model which predicts a decreasing color-singlet fraction with increasing $\Delta\eta$.

5.4 Color-Singlet Fraction Versus Parton x

5.4.1 Parton x of the $\Delta\eta$ Measurement

Finding the color-singlet fraction as a function of jet E_T, jet $\Delta\eta$ separation, and center-of-mass energy is an indirect measurement of its dependence on the initial parton x values. The slight increase in the color-singlet fraction with both increasing jet E_T and $\Delta\eta$ indicates that the color-singlet fraction may increase with increasing parton x. To study the x-range probed by the $\Delta\eta$ measurement, the two-dimensional color-singlet fraction is plotted in figure 5.11 as a function of the x values found from binning the data in $\Delta\eta$ (see table 5.2). The x values in this plot are determined using

equation 5.1 and include the values calculated using the high E_T data used in the $\Delta\eta$ measurement presented in reference [8] but not reproduced here.

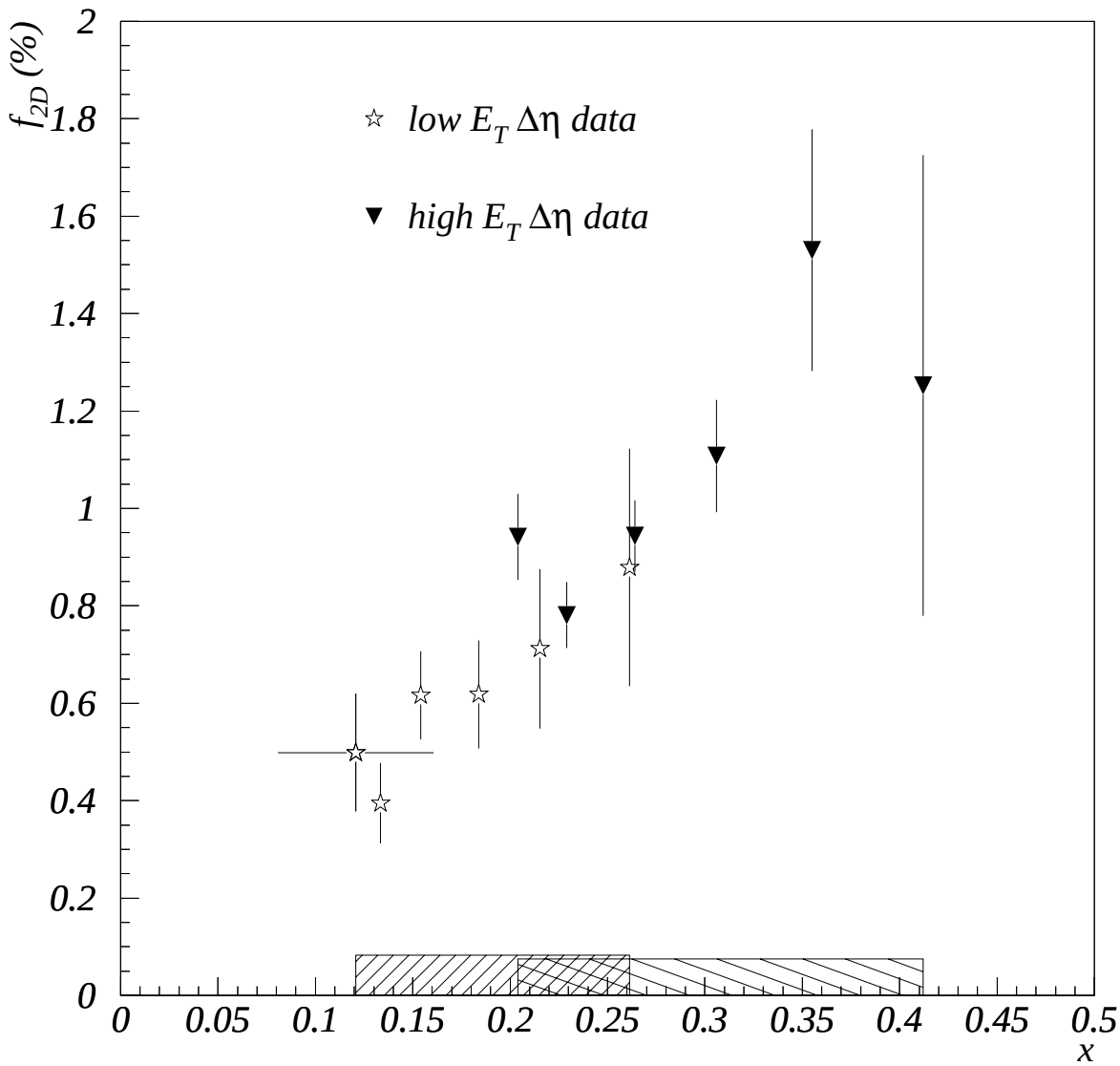

Figure 5.11. f^{2-D} as function of parton x using the $\Delta\eta$ data from the previous section. The points contain statistical error bars and each data set has a systematic normalization error band. The first point shows the width of the horizontal errors.

5.4.2 Various Parton x Definitions

The x definition given in equation 5.1 is an approximation of an average x value for each event. Rigorously, each of the two leading jets would be assigned an x value corresponding to its intial parton momentum fraction. Also, by definition, x calculations are generally meaningful for 2→2 processes, so summing over all jets in the event could inaccurately represent the average x value calculated. Therefore, it is of interest to measure the dependence of the rapidity gap fraction on x using more rigorous definitions and binning directly in x.

Several x definitions were studied:

- The average of x_a and x_b,

$$x_a = \sum_{i=1}^{2} \frac{E_{Ti}}{\sqrt{s}} e^{\eta_i} \tag{5.2}$$

$$x_b = \sum_{i=1}^{2} \frac{E_{Ti}}{\sqrt{s}} e^{-\eta_i} \tag{5.3}$$

$$< x_{a,b} > = (x_a + x_b)/2 \tag{5.4}$$

- The minimum of x_a and x_b,

$$x_{min} = min(x_a, x_b) \tag{5.5}$$

- The maximum of x_a and x_b,

$$x_{max} = max(x_a, x_b) \tag{5.6}$$

- The average of x_1 and x_2,

$$x_1 = \frac{E_{T1}}{\sqrt{s}} e^{|\eta_1|} \tag{5.7}$$

$$x_2 = \frac{E_{T2}}{\sqrt{s}} e^{|\eta_2|} \tag{5.8}$$

$$< x_{1,2} > = (x_1 + x_2)/2 \tag{5.9}$$

The 1800 GeV data was binned in x for each of these definitions and the fraction f^{2-D} was found. Background subtraction was not included since the background has been shown to be roughly independent of x (as seen in f_s^{2-D} versus dijet E_T and $\Delta\eta$ plots). Figure 5.12, shows f^{2-D} as a function of x using each definition. The fraction is shown to increase with increasing parton x regardless of the definition used.

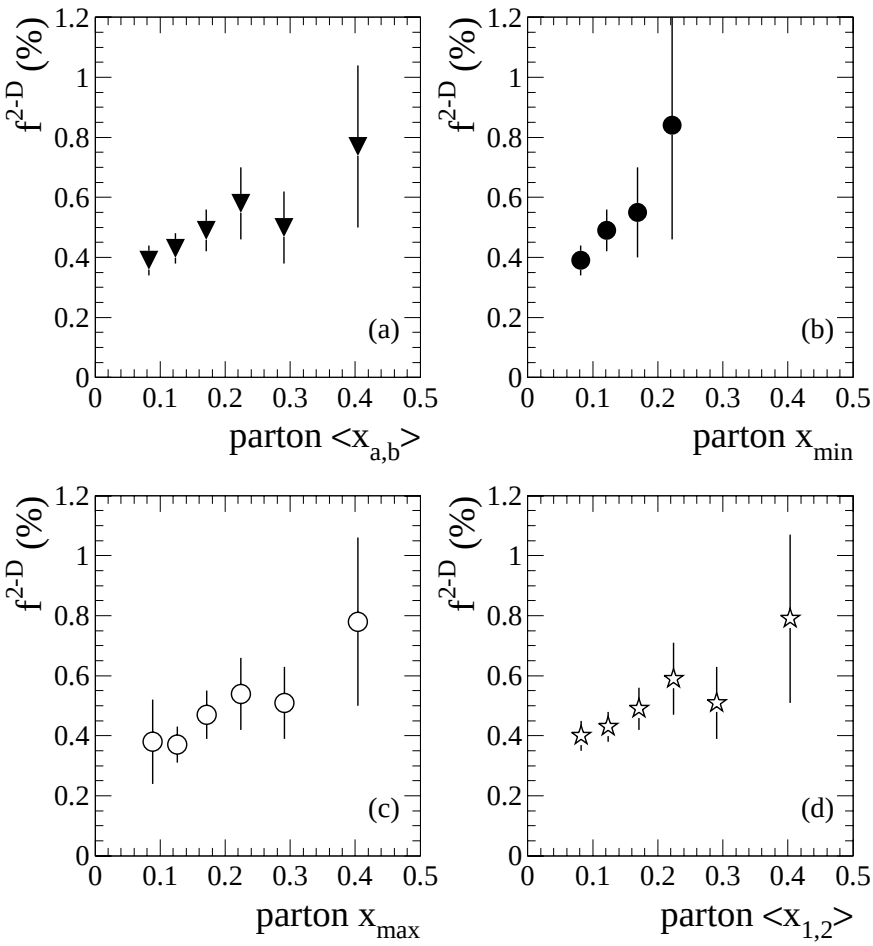

Figure 5.12. f^{2-D} as function of parton (a) $< x_{a,b} >$, (b) x_{min}, (c) x_{max}, and (d) $< x_{1,2} >$ for 1800 GeV data.

5.4.3 Parton x for 630 GeV Data

The 630 GeV data was also binned in x using the average of x_1 and x_2. Figure 5.13 shows the two-dimensional fraction versus $< x_{1,2} >$ for both the 630 GeV and 1800 GeV data. The 630 GeV data probes a higher x region than the 1800 GeV data, and the fractions are much higher than the 1800 GeV fractions. If the 630 GeV fractions are larger than the 1800 GeV fractions simply because of a different survival probability, the 630 GeV fractions can be normalized by the ratio of the two survival probabilities to verify whether the two center-of-mass values are in agreement.

The ratio of the survival probabilities at 630 GeV and 1800 GeV has recently been estimated to be $S_{630}/S_{1800} \cong 2.1$[7]. Figure 5.14 shows an overlay of the two-dimensional fraction versus $< x1,2 >$ for the 1800 GeV data and the 630 GeV data normalized lower by a factor of 2.1. Points for both data sets include statistical error bars. The normalized 630 GeV data is in good agreement with the 1800 GeV data, indicating that a possible explanation for the difference in the rapidity gap fractions at these two center-of-mass energies is simply due to differences in the survival probability. If, however, the survival probability is truly independent of the center-of-mass energy, an additional explanation of a difference in some other physical process would be needed to account for the differences in the rapidity gap fractions.

5.4.4 Interpretation of f^{2-D} vs. Parton x

All of the measurements of the color-singlet fraction versus parton x show that the color-singlet fraction rises with increasing x value, or increasing initial-state quark distributions. Again, these results are possibly consistent with the soft color rearrangement model for color-singlet exchange and are inconsistent with the naive two-gluon model.

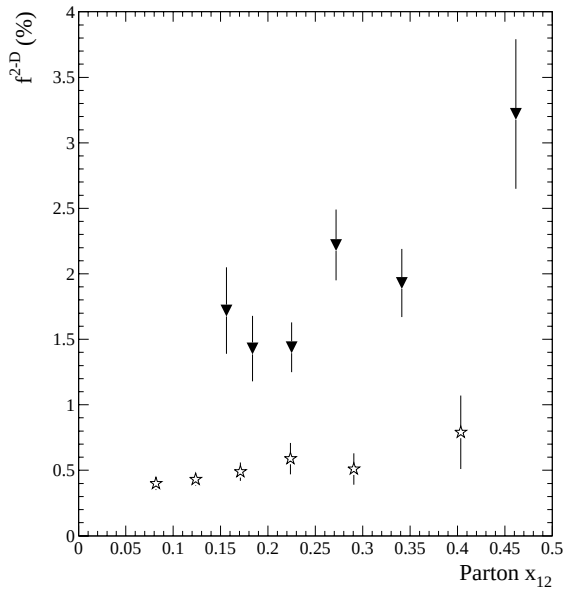

Figure 5.13. f^{2-D} as function of parton $\bar{x}$. Triangles are 630 GeV data; Stars are 1800 GeV data.

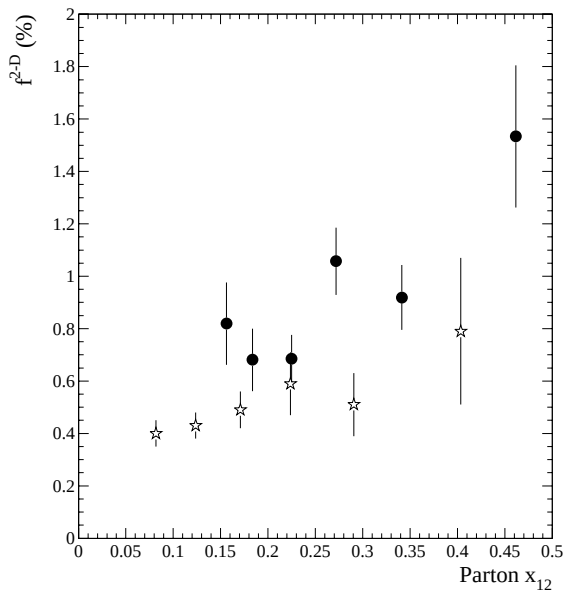

Figure 5.14. f^{2-D} as function of parton $\bar{x}$. Circles are normalized 630 GeV data; Stars are 1800 GeV data.

CHAPTER 6

CONCLUSIONS

The analysis presented in this dissertation probes the nature of strongly-interacting color-singlet exchange processes, providing insight into whether the color singlet preferentially couples to initial-state quarks or gluons. A color singlet that prefers a coupling to initial-state quarks will produce a rapidity gap fraction that increases with increasing initial quark distributions. A color singlet that prefers a coupling to initial state gluons will produce a rapidity gap fraction that decreases with increasing intial quark distributions. Several theoretical models currently exist to describe the dynamics of color-singlet exchange, and these models differ in that they predict different preferred couplings for the color-singlet object. The results of this analysis support color-singlet models that prefer initial-state quark processes.

The fraction of initial quarks increases with increasing parton x, which can be achieved by increasing the jet E_T, increasing the jet $\Delta\eta$ separation, or decreasing the center-of-mass energy. The rapidity gap fraction has been measured as a function of all of these variables, and the results are consistent with a color-singlet fraction that increases with increasing parton x. The results presented also suggest that the survival probability at $\sqrt{s} = 630$ GeV may be twice as large as that at 1800 GeV. This is in agreement with the current estimate for the dependence of the survival probability on center-of-mass energy [7].

These results are inconsistent with Bjorken's original simple two-gluon model for the color singlet and with the leading-log BFKL adaptation of this model. Because a two-gluon color singlet couples more strongly to initial gluons, both models predict

that the rapidity gap fraction should decrease with increasing jet E_T. The simple two-gluon model also predicts that the rapidity gap fraction should decrease with increasing jet $\Delta\eta$ separation, and decrease with decreasing center-of-mass energy. The results presented here in combination with those presented in reference [8] disagree with these predictions. The BFKL model differs from the simple two-gluon predictions in that it suggests that the rapidity gap fraction will increase with $\Delta\eta$ beyond some large undetermined $\Delta\eta$ value. In addition, BFKL dynamics do not change with center-of-mass energy and so there is no prediction. Both of these models are at leading order, and it is worth noting that the inclusion of higher order effects may give rise to predictions that are in better agreement with the data.

The results presented are possibly consistent with the predictions made by both the soft color rearrangement model and the U(1) gauge boson model. Both of these models predict a rapidity gap fraction that increases with increasing intial quark processes. The soft color rearrangement model qualitatively describes the data well. The agreement suggests that perhaps color-singlet exchange is not a product of the exchange of a perturbative color-singlet object but instead is a nonperturbative QCD effect arising from the cancellation of the color flowing between the scattered partons. The U(1) gauge boson model is interesting in that it proposes new physics to account for the observed rate of color-singlet exchange. As a photon-like object, the U(1) gauge boson couples only to quarks, producing an enhancement in the rapidity gap fraction with increasing parton x. Recent studies show, however, that the predicted rapidity gap fraction may rise much more steeply with increasing jet E_T than is observed in the data [10].

The measurements presented here and in reference [8] have challenged the historical models for color-singlet exchange and are stirring theoretical interest. It will

be interesting to see whether higher order calculations can revive the simple two-gluon model. Perhaps the addition of gluons will simply bridge the two-gluon and soft color rearrangement models. Or perhaps color-singlet exchange is not QCD at all but instead a signature for new physics.

BIBLIOGRAPHY

[1] J.D. Bjorken, Phys. Rev. Lett. **16**, 408 (1966);
J.D. Bjorken, Phys. Rev. **163**, 1767 (1967);
K. Gottfried, Phys. Rev. Lett. **18**, 1174 (1967);
R.P. Feynman, Phys. Rev. Lett. **23**, 1415 (1969).

[2] H.L. Lai et al., Phys. Rev. D **51**,4763 (1995);
H.L. Lai et al., Phys. Rev. D **55**, 1280 (1997).

[3] A.D. Martin, R.G. Roberts, and W.J. Sterling, Phys. Lett. B **356**, 89 (1995).

[4] R.S. Fletcher, private communication.

[5] J.D. Bjorken, Phys. Rev. D **47**, 101 (1993).

[6] E. Gotsman, E.M. Levin, and U. Maor, Phys. Lett. B **309**, 199 (1993).

[7] E. Gotsman, presented at Lishep '98 (1998).

[8] T. Thomas, Ph.D. Dissertation, Northwestern University, (1997) (unpublished).

[9] A. Brandt, et al., DØNote 3388, (1998) unpublished.

[10] A. Brandt, et al., DØNote 3389, (1998) unpublished.

[11] H. Chehime et al., Phys. Lett. B **286**, 397 (1992).

[12] V. Del Duca and W.K. Tang, Phys. Lett. B **312**, 225 (1993).

[13] H. Chehime and D. Zeppenfeld, MAD/PH-814 (1994).

[14] O.J.P. Éboli, E.M. Gregores, and F. Halzen, MADPH-96-965 (1996).

[15] Ya. Balitsky and L. Lipatov, Sov. J. Nucl. Phys. **28**, 822 (1978); L. Lipatov, Sov. Phys. JETP **63**, 904 (1986).

[16] C.D. Carone and H. Murayama, Phys. Rev. Lett. **74**, 3122 (1995).

[17] B. May, Ph.D. Dissertation, Univeristy of Arizona, (1994) (unpublished).

[18] DØ Collaboration, S. Abachi et al., Phys. Rev. Lett. **72**, 2332 (1994).

[19] DØ Collaboration, S. Abachi et al., Phys. Rev. Lett. **76**, 734 (1996).

[20] CDF Collaboration, F. Abe et al., Phys. Rev. Lett. **74**, 855 (1995).

[21] DØ Collaboration, S. Abachi et al., Nucl. Instrum. and Meth. A338, 185 (1994).

[22] Joey Thompson, "Introduction to Colliding Beams at Fermilab", Fermilab-TM-1909 (1994).

[23] N. Hadley, "Cone Algorithm for Jet Finding", DØNote 904 (1989) (unpublised).

[24] Jet energy scale group, "Jet Energy Scale (CAFIX 5.1)", DØNote 3139 (1996) (unpublised).

[25] D. Elvira et al., "Jet Energy Scale at DØ", DØNote 3287 (1997) (unpublished).

[26] R. Astur, J. Blazey, and D. Elvira, "A Study of Standard Jet Cuts and Their Efficiencies Using DØCollider Data", DØnote 1763 (1993) (unpublished).

[27] R. Astur, "Study of Fake Jets in the DØDetector", DØnote 1662 (1993) (unpublished).

[28] A. Milder, Ph.D. Dissertation, University of Arizona (1993) (unpublished).

[29] J. Bantly, Q. Li-Demarteau, "Multiple Interaction Tool", DØnote 1691 (1993) (unpublished).

[30] J. Bantly, "Multiple Interaction Tool Study", DØnote 1849 (1993) (unpublished).

[31] J. Pumplin, Phys. Rev. D **50**, 6811 (1994).

[32] I.M. Dremin, Report No. FIAN TD-6 (1994).